JEM Journal of Experimental Medicine

ARTICLE

Tumor-reactive LAG3^{+}CD8^{+} T cells diverge into terminally exhausted cells and long-lived memory T cells

Vaishali Aggarwal[1,2*], Yangxi Sun[1,2,3*], Chang Liu[1,2*], Jian Cui[1,2], Sasikanth Manne[4,5], Yingtong Dou[1,2,3], Qiang Chen[1,2], Erin A. Brunazzi[1,2], Kate M. Vignali[1,2], Haiguang Wang[1], E. John Wherry[4,5], Creg J. Workman[1,2], and Dario A.A. Vignali[1,2,6]

Chronic T cell stimulation in tumors and chronic viral infections leads to T cell exhaustion, a state of dysfunction. As LAG3 marks a prominent subset of exhausted T (T_{EX}) cells in mid-to-late stage tumors, we generated a *Lag3* lineage–tracing mouse model (*Lag3*^{iCreERT2}*Rosa26*$^{LSL\text{-}tdTomato}$) to fate map and characterize tumor-reactive LAG3^{+}CD8^{+} T_{EX} cells. In tumor-bearing mice, two distinct tumor-specific tdTomato^{+} CD8^{+} T cell subsets stratified by LAG3 surface expression (LAG3^{+}tdT^{+} and LAG3^{-}tdT^{+}) exhibited contrasting anatomical distributions, functionality and transcriptional profiles, yet shared TCR clonotypes, suggesting a common origin. While LAG3^{+}tdT^{+} CD8^{+} T_{EX} cells were restricted to the tumor microenvironment and predominantly terminally exhausted, LAG3^{-}tdT^{+} CD8^{+} T_{EX} cells were progenitors that persisted in vivo and are required for anti-tumor immunity against a secondary tumor challenge. This study highlights T_{EX} cell functional heterogeneity and plasticity and characterizes a unique fate-flexible LAG3^{-}tdT^{+} progenitor T_{EX} subset that drives an anti-tumor memory response, supporting antibody-based therapeutic targeting of LAG3^{+} T_{EX} cells to unleash anti-tumor immunity and promote durability.

Introduction

T cell exhaustion is driven by chronic T cell receptor (TCR) signaling and environmental pressures manifested in settings such as chronic viral infections and cancer, leading to a state of T cell dysfunction (Baessler and Vignali, 2024; Blank et al., 2019; Wherry and Kurachi, 2015). CD8^{+} exhausted T (T_{EX}) cells exhibit canonical transcriptional (Beltra et al., 2020; Giles et al., 2022; Wherry and Kurachi, 2015), epigenetic, and metabolic features (DePeaux and Delgoffe, 2021; Khan et al., 2019; Pauken et al., 2016; Satpathy et al., 2019; Sen et al., 2016) yet can be functionally heterogenous, exhibiting differential reprogrammability depending on their developmental stage and exposure to environmental signals (Philip and Schietinger, 2022). Inhibitory receptors (IRs) such as lymphocyte activation gene 3 (LAG3), programmed cell death protein 1 (PD1), and T cell immunoglobulin and mucin-domain containing-3 (TIM3; also known as hepatitis A virus cellular receptor 2) are expressed chronically by T_{EX} cells, which exhibit variable degrees of reinvigoration following immune checkpoint blockade (ICB) therapy (Blackburn et al., 2009; McLane et al., 2019). Notably, differential response to ICB is believed to be attributed to phenotypic and functional heterogeneity among CD8^{+} T_{EX} cells (Huang et al., 2022; Miller et al., 2019; Paley et al., 2012; Schietinger et al., 2016; Utzschneider et al., 2016).

Distinct subsets of CD8^{+} T_{EX} cells differentially mediate control and response to ICB in chronic viral infection (Beltra et al., 2020; Daniel et al., 2022; Utzschneider et al., 2016) and cancer (Huang et al., 2022; Miller et al., 2019; Sade-Feldman et al., 2019; Schietinger et al., 2016). In chronic viral infection, terminally exhausted CD8^{+} T cells co-express IRs such as PD1 and TIM3, whereas progenitor stem-like CD8^{+} T_{EX} cells express intermediate levels of PD1 and CXCR5 (Im et al., 2016; Paley et al., 2012). These dysfunctional T cell states demonstrate a developmental hierarchy based on LY108 (*SLAMF6*) and CD69 expression, highlighting epigenetic and transcriptional dynamics across T_{EX} transitional states (Beltra et al., 2020) and divergent

[1]Department of Immunology, University of Pittsburgh School of Medicine, Pittsburgh, PA, USA; [2]Tumor Microenvironment Center, UPMC Hillman Cancer Center, Pittsburgh, PA, USA; [3]Cellular and Molecular Pathology Program, University of Pittsburgh School of Medicine, Pittsburgh, PA, USA; [4]Institute for Immunology and Immune Health, Perelman School of Medicine, University of Pennsylvania, Philadelphia, PA, USA; [5]Department of Systems Pharmacology and Translational Therapeutics, Perelman School of Medicine, University of Pennsylvania, Philadelphia, PA, USA; [6]Cancer Immunology and Immunotherapy Program, UPMC Hillman Cancer Center, Pittsburgh, PA, USA.

*V. Aggarwal, Y. Sun, and C. Liu contributed equally to this paper. Correspondence to Dario A.A. Vignali: dvignali@pitt.edu

C. Liu's current affiliation is Institute of Modern Biology, Nanjing University, Nanjing, Jiangsu, China. H. Wang's current affiliation is Department of Integrative Biology and Physiology, University of Minnesota, Minneapolis, MN, USA. D.A.A. Vignali is the lead contact.

clonal differentiation trajectories among late T_{EX} subsets (Daniel et al., 2022). Additionally, *TOX*, a key driver of T_{EX} epigenetic reprogramming, coordinates development and dynamics of T_{EX} subsets through regulation of *TCF1* and *T-BET* (*TBX21*) (Beltra et al., 2020; Bordon, 2019; Khan et al., 2019). Analogous to viral infection, $CD8^+$ T_{EX} cells in tumors have a subpopulation of progenitor exhausted cells ($LY108^+TIM3^-$) that mediate response to anti-PD1 therapy, persist long-term, retain polyfunctionality, and differentiate into terminally T_{EX} cells (Chen et al., 2019; Huang et al., 2022; Im et al., 2016; Liu et al., 2023; Miller et al., 2019; Siddiqui et al., 2019). Distinct markers are used across different studies to define $CD8^+$ T_{EX} subsets, highlighting the heterogenous developmental landscape of T_{EX} cells and gaps in our understanding of their relationship, underlying mechanisms, and functionality.

Limited analysis has characterized the fate and function of T_{EX} heterogeneity (Buchholz et al., 2016). This is partly due to the lack of key markers or tools to fate map T_{EX} cells. LAG3 is an important IR that has been successfully targeted in the clinic and is expressed on more terminally differentiated T_{EX} subsets across multiple tumor types (Andrews et al., 2020; Grosso et al., 2009; Lucas et al., 2011; Tawbi et al., 2022; Woo et al., 2012). Functionally, LAG3 expressed by $CD8^+$ T cells is critical to maintain tolerance to self and tumor antigens (Grosso et al., 2007). In mid- to late-stage tumor-bearing mice, the preponderance of LAG3 expression within the $CD8^+$ T cells compartment is on T_{EX} cells, facilitating the use of LAG3 as a marker to trace their fate. Hence, evaluating the longitudinal trajectory of $LAG3^+$ $CD8^+$ T_{EX} cells could offer new insights into the fate and function of T_{EX} cells.

We generated a LAG3 lineage–tracing tool, $Lag3^{iCreER-T2}Rosa26^{LSL\text{-}tdTomato}$ mice, to fate map and characterize the population dynamics of *Lag3* transcriptional active $CD8^+$ T cells and their progenies marked by tandem-dimer Tomato fluorescent protein $(tdT)^+$ cells across multiple tumor models. We identified two distinct tdT^+ $CD8^+$ T cell subsets, identified by tdTomato (tdT) and differential LAG3 cell surface expression ($LAG3^+tdT^+$ and $LAG3^-tdT^+$), that have shared TCR clonotypes, suggesting a common origin. Single-cell RNA-sequencing (scRNAseq) and ATAC sequencing of polyclonal $CD8^+$ T cells suggested that both spatial and temporal cues play an important role in shaping the fate of tdT^+ cells. $LAG3^+tdT^+$ $CD8^+$ T_{EX} cells predominantly exhibited a terminal exhaustion associated phenotype and are restricted to the tumor microenvironment (TME). In contrast, $LAG3^-tdT^+$ $CD8^+$ T_{EX} cells leave the tumor as stem-like progenitor cells that persisted in vivo, forming part of the peripheral tumor-specific memory pool, and retain the capacity to generate $LAG3^+tdT^+$ $CD8^+$ T_{EX} cells that contribute to secondary tumor clearance. Taken together, our findings define the functional heterogeneity of $Lag3^+$ $CD8^+$ T_{EX} cells and identify a unique subset of $LAG3^-tdT^+$ $CD8^+$ T_{EX} cells that is fate flexible and mediates long-term tumor control.

Results

$Lag3^{iCreERT2}Rosa26^{LSL\text{-}tdTomato}$: A temporally controlled Cre line to fate map $LAG3^+$ T_{EX} cells

We generated a tamoxifen-inducible $Lag3^{iCreERT2}$ mouse line to longitudinally fate map and evaluate the function of $Lag3^+$ T_{EX} cells. LAG3 was chosen because it is consistently a signature marker associated with tumor-reactive T_{EX} across human and murine tumor types (Aggarwal et al., 2023; Andrews et al., 2017; Andrews et al., 2022). The $Lag3^{iCreERT2}$ line was generated by inserting an iCreERT2 cassette into the endogenous *Lag3* locus at the translational start site, linked via a 2A peptide to generate a single multicistronic transcript (Szymczak et al., 2004). This design couples LAG3 and CreERT2 expression, restricting recombination to cells expressing *Lag3* at the time of tamoxifen administration. In contrast to IRES-based or transgenic systems, in which reporter expression can be uncoupled from the endogenous locus, in our model CreERT2 expression is directly linked to *Lag3* transcription. This line was crossed to $Rosa26^{LSL\text{-}tdT}$ to report Cre activity via tdT expression and facilitate fate-mapping of $Lag3^+$ cells in vivo (Fig. 1 A).

To evaluate both Cre recombination efficiency and optimal timing to initiate tdT expression, we treated mice with a series of 3-day tamoxifen dosing schemes using the B16-F10 melanoma model (Fig. 1 B). Intratumoral T cells had the highest tdT expression following day 8–10 (d8–10) tamoxifen treatment, and the expression was most prominent in $CD8^+$ T cells compared with $CD4^+$ conventional T (T_{conv}) and regulatory T (T_{reg}) cells (Fig. 1, C and D). A similar pattern was observed in the periphery albeit with a considerably lower percentage of tdT-positive cells (Fig. S1 A). We also assessed the stability of LAG3 expression on tdT^+ cells. A substantial proportion of tdT^+ $CD8^+$ T cells did not express surface LAG3 and were only tdT^+ (Fig. 1 E). Additionally, across all conditions, there was minimal tdT expression in the vehicle control groups, suggesting that the expression was tightly controlled. Analyses of the spleen, non-draining LNs (NDLNs), and draining LNs (DLNs) are shown in Fig. S1 B. Finally, given that tamoxifen treatment on d8–10 after tumor inoculation induced the highest tdT expression, this treatment scheme was chosen to evaluate the fate of $LAG3^+tdT^+$ and $LAG3^-tdT^+$ $CD8^+$ T cells in all subsequent experiments.

Next, we assessed the specificity of tdT labeling by treating one group with PBS instead of B16-F10 melanoma cells, while both groups received tamoxifen from d8 to d10 (Fig. S1 C). Analysis of the spleen and LNs revealed a small percentage of tdT^+ cells in the PBS group, reflecting baseline Cre activation under tamoxifen induction in the absence of tumor. We anticipate that this background labeling may be due to the low frequency of microbiota-reactive T cells that are generated at mucosal sites at steady state (Honda and Littman, 2016; Yang and Cong, 2021). The elevated PD1 expression observed on tdT^+ cells in tumor-baring mice may reflect activation of tumor reactive T cells that disseminate in the periphery (Fig. S1 D).

To define the population dynamics of $LAG3^+tdT^+$ and $LAG3^-tdT^+$ cells, we analyzed NDLNs, DLNs, and tumors at three time points (Fig. 2 A). $LAG3^+tdT^+$ cells were abundant in tumor-infiltrating lymphocytes (TILs) but were absent in the periphery, indicating their restriction to the TME. $LAG3^-tdT^+$ cells were present in both TILs and the periphery, with a higher frequency in TILs, although their overall abundance remained low in both compartments (Fig. 2, B and C). Analysis of PD1 expression revealed that the $LAG3^+tdT^+$ subset exhibited a $PD1^{hi}LAG3^{hi}$ phenotype, while the $LAG3^-tdT^+$ cells were

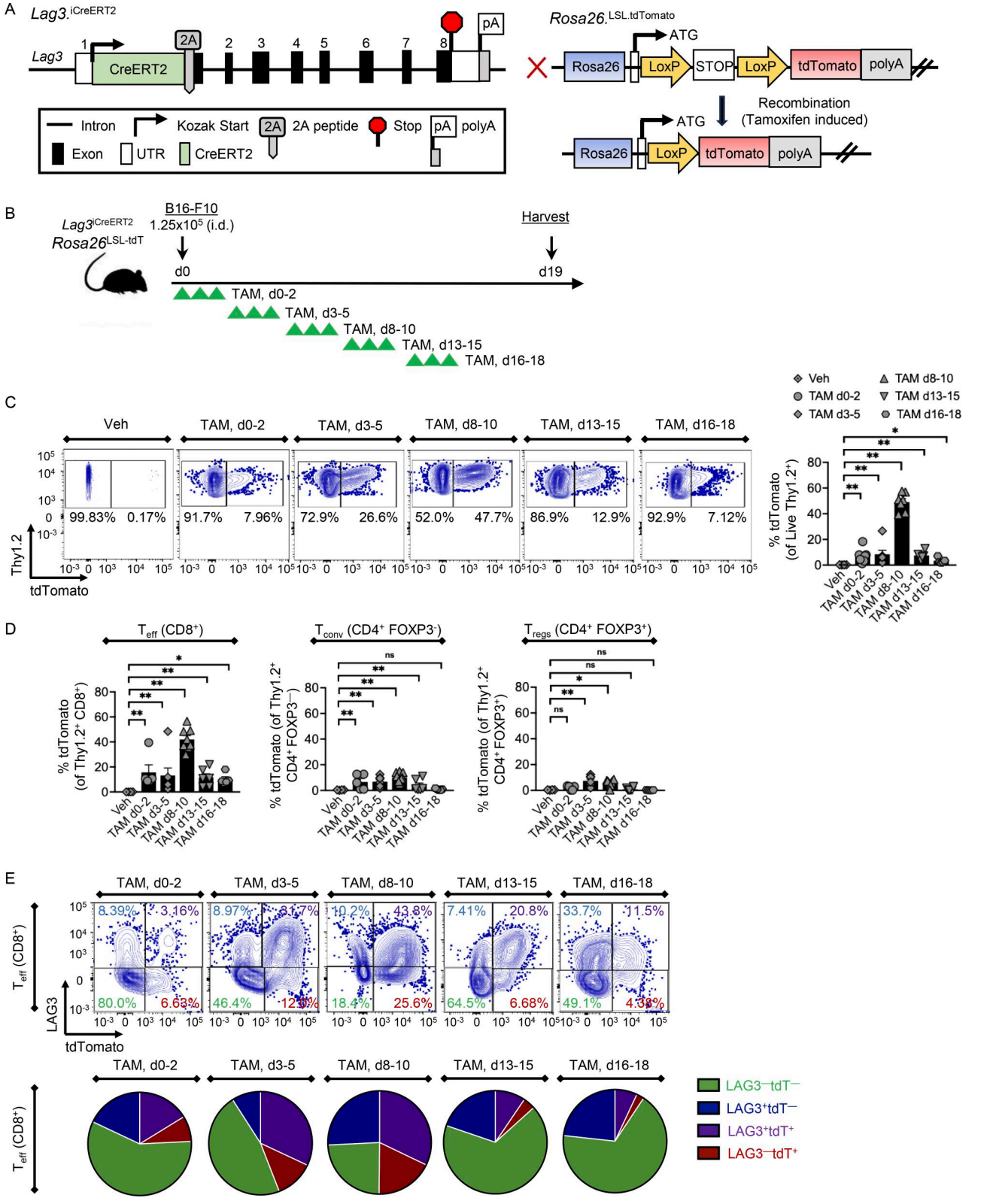

Figure 1. **Generation of a tamoxifen-inducible LAG3⁺ cell–specific fate-mapping Cre line. (A)** Schematic of the *Lag3*^{iCreERT2} *Rosa26*$^{LSL\text{-}tdTomato}$ mouse. **(B)** B16-F10 tumor implanted in *Lag3*^{iCreERT2} *Rosa26*$^{LSL\text{-}tdT}$ mice, treated with three daily tamoxifen injections (2 mg in 5% EtOH/sunflower oil) in a time-course–dependent manner (d0–2, d3–5, d8–10, d13–15, and d16–18), and harvested on d19. A subset of mice was given 5% EtOH/sunflower oil as vehicle (Veh) control. **(C)** Lymphocytes were isolated from tumors, and tdT expression was assessed on the T cell compartment to identify the best labeling scheme to capture tdT⁺ cells, gated on Thy1.2⁺ T cells. **(D)** tdT expression was assessed on CD8⁺, T_{conv} (CD4⁺ FOXP3⁻), and T_{reg} (CD4⁺ FOXP3⁺) cells in tumors treated with tamoxifen, gated on Thy1.2⁺ T cells. **(E)** LAG3 and tdT expression was assessed on CD8⁺ T cells isolated from B, gated on Thy1.2⁺ CD8⁺ T cells. Proportion of respective LAG3⁻tdT⁻, LAG3⁺tdT⁻, LAG3⁺tdT⁺, and LAG3⁻tdT⁺ CD8⁺ T cells recovered from B16-F10 tumor at d19. Data in C–E are from $n = 5–8$ mice for each group, pooled from three independent experiments. *P < 0.05; **P < 0.01; ns, not significant by unpaired *t* test (C and D). Error bars represent mean ± SEM.

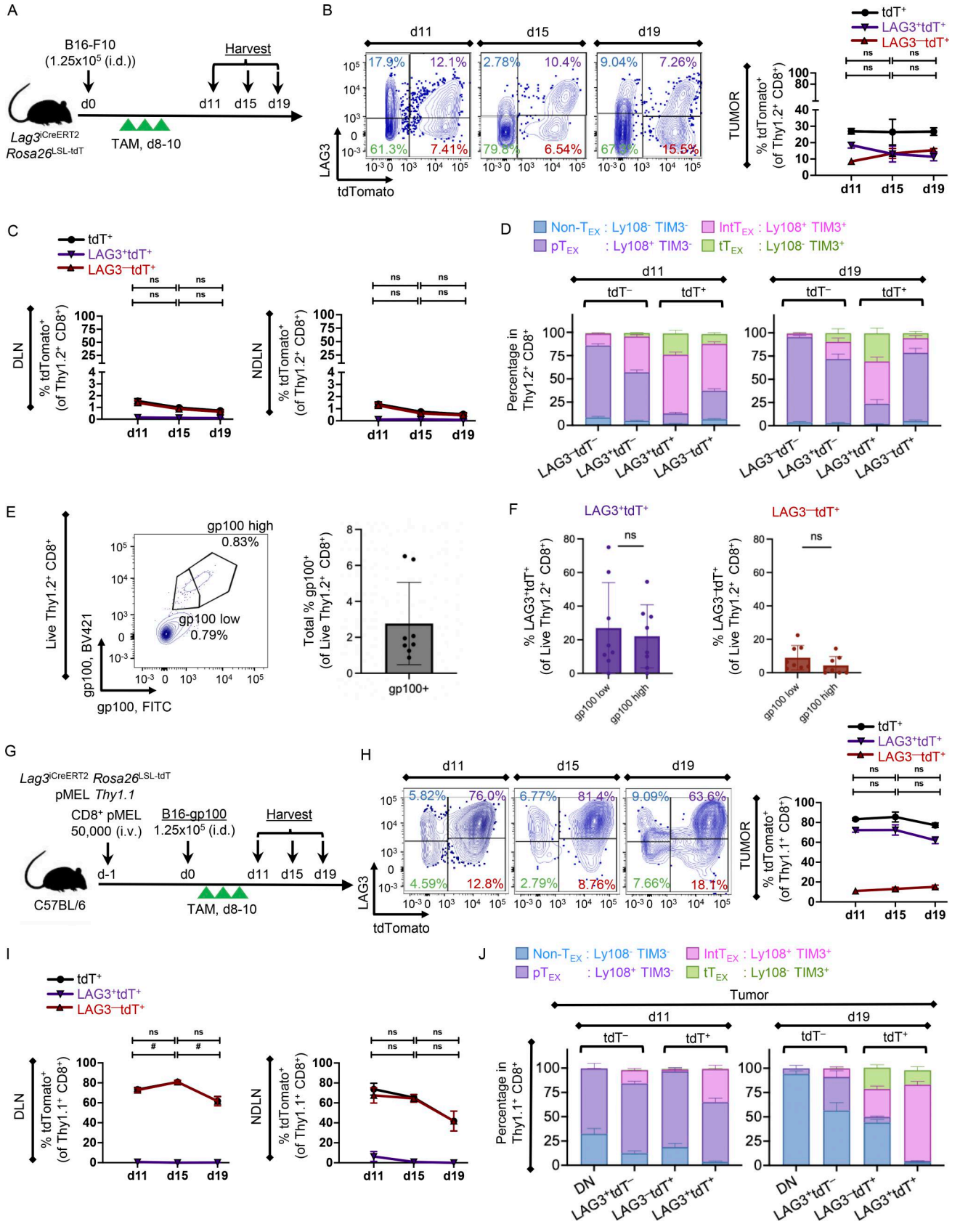

Figure 2. **The LAG3⁻tdT⁺ CD8⁺ T_{EX} cells are found in periphery compared with the LAG3⁺tdT⁺ CD8⁺ T_{EX} cells, which are more terminally T_{EX} and restricted to tumor compartment. (A)** Scheme for evaluation of population kinetics of tdT⁺ cells in tumor-bearing host. *Lag3*^{iCreERT2} *Rosa26*$^{LSL\text{-}tdT}$ mice were i.d. implanted with melanoma cells (1.25×10^5), treated with three tamoxifen injections (2 mg in 5% EtOH/sunflower oil) at d8–10, and harvested on d11, d15,

and d19. **(B and C)** LAG3 and tdT expression was assessed on CD8⁺ T cells isolated from (B) B16-F10 tumors and (C) DLNs and NDLNs, gated on Thy1.2⁺ CD8⁺ T cells. **(D)** LY108 and TIM3 expression on different tdT subsets. Phylum plot represents the percentage of LY108⁻TIM3⁻ (blue), LY108⁺TIM3⁻ (purple), LY108⁺TIM3⁺ (pink), and LY108⁻TIM3⁺ (green) CD8⁺ T cells. **(E)** gp100⁺ cells were assessed on CD8⁺ T cells isolated from tumor on d18 of *Lag3*^{iCreERT2}*Rosa26*$^{LSL\text{-}tdT}$ mice implanted with B16gp100 and treated with three tamoxifen injections (2 mg in 5% EtOH/sunflower oil) d8–10. **(F)** LAG3 and tdT expression were evaluated in both gp100 high and gp100 low populations. **(G)** Schematic representation of *Lag3*^{iCreERT2} *Rosa26*$^{LSL\text{-}tdT}$ pMEL-T cells (50,000 Thy1.1⁺CD8⁺ T cells) injected i.v. into C57BL/6 mice on d−1 followed by i.d. injection of B16gp100 tumor cells (1.25×10^5) on d0, treated with three tamoxifen injections (2 mg in 5% EtOH/sunflower oil) at d8–10, and harvested on d11, d15, and d19. **(H and I)** LAG3 and tdT expression was assessed on Thy1.1⁺ CD8⁺ T cells isolated from B16gp100 tumors (H), DLNs and NDLNs (I), gated on Thy1.1⁺ CD8⁺ T cells. **(J)** LY108 and TIM3 expression on different tdT subsets. Data in B–D and H–J are from n = 6–10 mice per group, pooled from three independent experiments. Data in E and F are representative of two independent experiments with n = 8 mice. Statistical analysis of LAG3⁺tdT⁺ and LAG3⁻tdT⁺ CD8⁺ T cells from d11–15 and d15–19 are represented by * and #, respectively. #P < 0.05; ns, not significant, by two-way ANOVA (B, C, H, and I) or unpaired t test (F). Error bars represent mean ± SEM.

primarily PD1$^{int/hi}$ (Fig. S1 E). The exhausted phenotype of these tdT⁺ cells was investigated using LY108 (*Slamf6*) and TIM3. LAG3⁺tdT⁺ CD8⁺ T cells presented a more intermediate and terminal exhausted phenotype, whereas the LAG3⁻tdT⁺ CD8⁺ T cells both in the TME and peripheral express markers associated with the progenitor exhausted state (Fig. 2 D and Fig. S1, F and G). The LAG3⁻tdT⁻ population also contained a substantial LY108⁺TIM3⁻ fraction. The identification of LAG3⁻tdT⁺ progenitor-like cells suggests that expression of LAG3 is not restricted to terminally exhausted CD8⁺ T cells. Rather, a fraction of progenitor cells can express LAG3 and subsequently persist as a progenitor-like population after downregulate surface LAG3. Together, these data suggest that a subpopulation of LAG3⁺tdT⁺ CD8⁺ T cells loses surface LAG3 expression early during tumor progression and presents a progenitor exhausted phenotype, potentially positioning them to circulate more broadly. In contrast, more T_{EX} cells appeared to be tumor resident.

We next examined whether differences in TCR affinity could account for the distribution and phenotypic differences of LAG3⁺tdT⁺ and LAG3⁻tdT⁺ CD8⁺ T cells. Comparing their frequencies within gp100 tetramer high and tetramer low populations, there are no significant differences in the distribution of these two subsets (Fig. 2, E and F). These results indicate that the dynamics of LAG3⁺tdT⁺ and LAG3⁻tdT⁺ CD8⁺ T cell cannot be explained simply by differences in TCR affinity but rather reflect additional mechanisms influencing their fate.

We characterized the population kinetics of these two tdT⁺ subsets in three additional tumor models, including the YUMM1.7 and YUMMER1.7 melanoma models, and the MC38 colon adenocarcinoma model. Consistent with our findings in the B16-F10 and B16-gp100 models, the LAG3⁺tdT⁺ subset of CD8⁺ T_{EX} cells remained restricted to the TME across all five tumor models, whereas LAG3⁻tdT⁺ CD8⁺ cells were essentially the only tdT⁺ subset detected in the periphery (Fig. S2, A–F).

To assess the trajectory of these tdT⁺ T_{EX} cells in a monoclonal CD8⁺ T cell population, we crossed *Lag3*^{iCreERT2}*Rosa26*$^{LSL\text{-}tdT}$ mice with gp100-specific pMEL TCR transgenic mice on a *Rag1*$^{-/-}$ background (Fig. 2 G). Consistently, both LAG3⁺tdT⁺ and LAG3⁻tdT⁺ CD8⁺ T cells were found in the adoptively transferred pMEL–T cells from the B16-gp100 tumor-bearing host, with LAG3⁺tdT⁺ CD8⁺ T cells being the dominant tdT⁺ population in the TME, while LAG3⁻tdT⁺ T cells were the only subpopulation in the periphery (Fig. 2, H and I). LAG3⁻tdT⁺ CD8⁺ T cells presented a more progenitor exhausted phenotype compared with the intermediate exhausted phenotype of LAG3⁺tdT⁺ cells (Fig. 2 J).

Using this model, we were also able to assess the correlation between antigen specificity and the generation of tdT⁺ cells. Dual inoculation with B16-gp100 and antigen-irrelevant MC38 tumors revealed that tdT⁺ cells were nearly undetectable in MC38 tumors and corresponding DLNs, whereas they accumulated at significantly higher frequencies in B16-gp100 tumors (Fig. S2, G–I).

Taken together, we established an inducible Cre mouse strain that marks *Lag3*⁺ T_{EX} cells with high fidelity. Using *Lag3*^{iCreERT2}*Rosa26*$^{LSL\text{-}tdT}$ mice, we identified two unique subsets of tdT⁺ CD8⁺ T_{EX} cells with differential LAG3 surface expression (LAG3⁺tdT⁺ and LAG3⁻tdT⁺), with the former restricted to the TME and the latter found to variable degrees in the TME as well as in the periphery.

Temporal and spatial cues shape the fate of tdT⁺ cells

To interrogate the lineage relationship between intratumoral and peripheral tdT⁺ subsets, we performed scRNAseq and paired single-cell TCR sequencing (scTCRseq) of intratumoral LAG3⁻tdT⁻, LAG3⁺tdT⁺, and LAG3⁻tdT⁺ CD8⁺ T cells, as well as peripheral CD44⁺tdT⁻ and CD44⁺tdT⁺ CD8⁺ T cells from B16-F10 tumor-bearing mice on d11 and d19 in *Lag3*^{iCreERT2}*Rosa26*$^{LSL\text{-}tdT}$ mice (Fig. 3 A). To enhance repertoire coverage, TCRseq data were further complemented with TRUST4 analysis. Since LAG3⁺ cells are detectable rarely in the periphery, we used CD44 as a surrogate marker. This allowed us to infer that CD44⁺ tdT⁺ cells share features of peripheral LAG3⁻tdT⁺ cells.

We quantified clonal expansion by assessing the frequency of cells bearing identical TCRs within each subset. Clones that had expanded >10-fold were classified as "high expansion," whereas those below this threshold were considered "low expansion." At day 11 (d11), intratumoral LAG3⁺tdT⁺ and LAG3⁻tdT⁺ CD8⁺ T_{EX} cells exhibited comparable proportions of highly expanded clones within their respective populations. At day 19 (d19), the LAG3⁺tdT⁺ cells displayed a further increase in clonal expansion. Notably peripheral CD44⁺tdT⁺ CD8⁺ T_{EX} cells also demonstrated a progressive increase in high-expansion clones over time (Fig. 3 B). We next tracked the common highly expanded TCR clones among LAG3⁺tdT⁺ and LAG3⁻tdT⁺ CD8⁺ T_{EX} cells in the tumor and CD44⁺tdT⁺ cells in the periphery to determine the extent of clonal sharing and potential lineage relationships between these subsets. At d11, 20% of the peripheral CD44⁺tdT⁺ CD8⁺ T cell clonotypes were shared with both intratumoral LAG3⁺tdT⁺ and

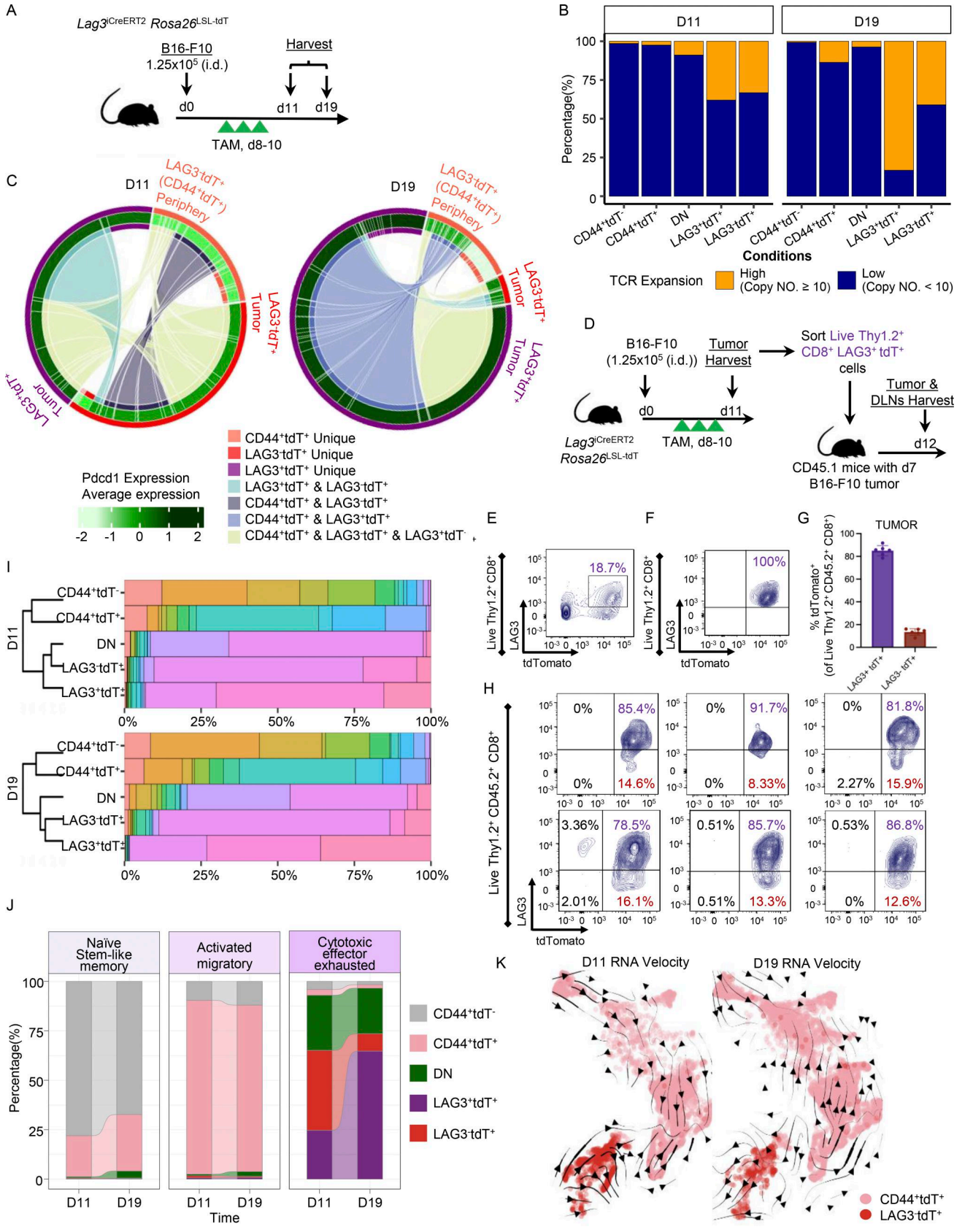

Figure 3. **Temporal and spatial cues shape the fate of tdT⁺ cells. (A)** scRNAseq analysis of tdT subsets in the tumor and periphery on d11 and d19 following i.d. injection of *Lag3*^{iCreERT2}*Rosa26*$^{LSL\text{-}tdT}$ mice with 1.25 × 10^5 B16-F10 melanoma cells. **(B)** TCR clonal expansion of indicated CD8⁺ T cell subsets at d11 and d19, showing proportions of highly expanded (≥10 copies) versus lowly expanded (<10 copies) clones. **(C)** Circos plots showing the distribution of highly expanded

clones and PD1 expression across tumor-infiltrating and peripheral CD8⁺ T cell subsets at d11 (left) and d19 (right), highlighting clones that are unique to individual subsets versus those shared across multiple subsets. **(D)** Schematic overview of the adoptive transfer strategy. LAG3⁺tdT⁺ CD8⁺ T cells were isolated from d11 B16-F10 tumors of *Lag3*^{iCreERT2} *Rosa26*$^{LSL\text{-}tdT}$ (Thy1.2⁺ CD45.2⁺) mice and intratumorally transferred 3–4 × 10^3 cells into CD45.1⁺ recipient mice bearing established d7 B16-F10 tumors. Recipient tumors and DLNs were harvested at d12 for flow cytometric analysis. **(E)** Representative flow cytometry plot showing the gating strategy for identification and sorting of LAG3⁺tdT⁺ CD8⁺ T cells from d11 tumors of *Lag3*^{iCreERT2} *Rosa26*$^{LSL\text{-}tdT}$ mice. **(F)** Representative flow cytometry plot confirming the purity of the post-sort LAG3⁺tdT⁺ CD8⁺ T cell population. **(G)** Summary bar graph showing the frequencies of LAG3⁺tdT⁺ and LAG3⁻tdT⁺ CD8⁺ T cells, quantified from the individual tumors shown in H. **(H)** Representative flow cytometry plots of six individual recipient tumors at d12 following intratumoral adoptive transfer. Results are from three independent experiments. **(I)** Distribution of transcriptional clusters within each tdT subset at d11 (top) and d19 (bottom). Hierarchical clustering reflects relationships among subsets based on cluster composition ratio. **(J)** Cell ratio shifting on temporal dynamics of naive/stem-like memory, activated/migratory, and cytotoxic effector/exhausted programs across tdT subsets. **(K)** RNA velocity streamlines projected onto UMAP at d11 and d19, showing predicted trajectories between single-positive tdT⁺ subsets, with tumor-infiltrating LAG3⁻tdT⁺ (red) and peripheral CD44⁺tdT⁺ (pink) cells highlighted. Data in B and C and I–K are representative of two independent experiments. Error bars represent mean ± SEM.

intratumoral LAG3⁻tdT⁺ CD8⁺ T cell, while 50% overlapped with intratumoral LAG3⁻tdT⁺ alone. By d19, 40% of peripheral CD44⁺tdT⁺ clonotypes were shared with 60% of intratumoral LAG3⁺tdT⁺ clonotypes, whereas the set of clonotypes shared exclusively with intratumoral LAG3⁻tdT⁺ declined to nearly 0% (Fig. 3 C and Fig. S3 A). The distribution of different TCR abundances is shown in Fig. S3 B. Given the increased PD1 protein expression observed on peripheral LAG3⁻tdT⁺ CD8⁺ T cells in tumor-bearing mice compared with PBS controls (Fig. S1 D), we next assessed if there was any relationship between *Pdcd1* transcript levels and whether TCR clonotypes were shared. Essentially all of the TCR clones with elevated *Pdcd1* expression on peripheral LAG3⁻tdT⁺ CD8⁺ (CD44⁺tdT⁺) T cells at d19 were shared with tumoral tdT⁺ CD8⁺ T cells, whereas unshared clones exhibited comparatively low *Pdcd1* transcript levels (Fig. 3 C). Together, these data suggest that a substantial proportion of peripheral CD44⁺tdT⁺ cells originated from intratumoral LAG3⁺tdT⁺ CD8⁺ T cells, supporting a lineage relationship between these tdT⁺ populations.

To further test this lineage relationship, we performed an adoptive transfer experiment (Fig. 3 D). LAG3⁺tdT⁺ CD8⁺ T cells were sorted from d11 tumors (Fig. 3, E and F) from CD45.2⁺ *Lag3*^{iCreERT2}*Rosa26*$^{LSL\text{-}tdT}$ mice and intratumorally transferred into CD45.1⁺ recipient mice bearing day 7 (d7) tumors. Upon analysis of recipient tumors at day 12 (d12), donor LAG3⁺tdT⁺ CD8⁺ T cells maintained a LAG3⁺tdT⁺ compartment but importantly also gave rise to a LAG3⁻tdT⁺ population (Fig. 3, G and H), indicating that a subset of LAG3⁺tdT⁺ CD8⁺ T cells can transition to a LAG3⁻tdT⁺ state. Notably, donor-derived cells were also detected in the DLNs in a subset of recipients (2/6 mice), as well as in the NDLNs (1/6 mice) and spleen (1/6 mice), and these cells were exclusively LAG3⁻tdT⁺.

The unsupervised clustering analysis of the scRNAseq data identified 15 clusters with distinct transcriptional signatures across all subsets, which were subsequently grouped into three functional categories: (1) naive/stem-like memory, (2) cytotoxic effector/exhausted, and (3) activated/migratory (Fig. S3, C and D). We constructed a dendrogram using hierarchical clustering of functional cluster distributions to illustrate the relative relationships across different subsets over time. At the early time point, intratumoral LAG3⁻tdT⁺ CD8⁺ T cells showed greater transcriptional proximity to intratumoral LAG3⁻tdT⁻ CD8⁺ T cells, whereas at the late time point, intratumoral LAG3⁻tdT⁺ CD8⁺ T cells clustered more closely with intratumoral LAG3⁺tdT⁺ cells (Fig. 3 I). In addition, the proportion of exhausted intratumoral LAG3⁻tdT⁺ cells declined over time, accompanied by a reciprocal increase of intratumoral LAG3⁺tdT⁺ cells. In contrast, peripheral CD44⁺tdT⁺ CD8⁺ cells exhibited a progressive gain of naive/stem-like memory-associated features (Fig. 3 J). Additional UMAP analysis focusing specifically on intratumoral subsets revealed substantial, albeit not complete, overlap among the LAG3⁺tdT⁺ and LAG3⁻tdT⁺ cells within the tumor (Fig. S3 E).

RNA velocity analysis was applied to infer developmental trajectories across single positive cells. At d11, velocity vectors suggested a directional flow from intratumoral LAG3⁻tdT⁺ cells toward peripheral CD44⁺tdT⁺ cells, indicating a potential ongoing transition. By d19, vectors were primarily oriented within the peripheral CD44⁺tdT⁺ cell population itself, consistent with the stabilization of peripheral CD44⁺tdT⁺ cells following this transition (Fig. 3 K). Together, these data indicate a coordinated temporal and spatial shift in tdT⁺ CD8⁺ T cell functional states. By evaluating transcriptional expression of both *Lag3* and *Adam10* across all tdT⁺ subsets, we can further assess whether loss of LAG3 expression in LAG3⁻tdT⁺ cells was due to transcriptional downregulation or other regulatory mechanisms, such as membrane shedding mediated by Adam10. We observed that LAG3⁺tdT⁺ CD8⁺ T_{EX} cells had the highest intratumoral expression of *Lag3* and *Adam10*, whereas LAG3⁻tdT⁺ cells in the periphery showed substantial *Adam10* expression but lacked detectable *Lag3* transcripts in the scRNAseq data (Fig. S3 F). This suggests that LAG3 is not being transcribed in LAG3⁻tdT⁺ cells, rather than being lost through proteolytic shedding. Nonetheless, further studies are needed to gain deeper mechanistic insights into the development and regulation of these LAG3⁻tdT⁺ CD8⁺ T_{EX} cells.

Epigenetic and functional divergence of intratumoral and peripheral tdT⁺ cells

To further dissect lineage relationship and whether transcriptional trajectories are underpinned by epigenetic regulation, we performed transposase-accessible chromatin with sequencing (ATACseq) at d19 to investigate whether the observed transcriptional dynamics were accompanied by changes in chromatin accessibility (Fig. 4 A). We then assessed the high variable peaks with groups with Pearson correlation coefficient analysis, which revealed a high similarity index between intratumoral LAG3⁺tdT⁺ and LAG3⁻tdT⁺ CD8⁺ T_{EX} cells on d19. In contrast, peripheral LAG3⁻tdT⁺ CD8⁺ T cells had already diverged from

intratumoral LAG3⁻tdT⁺ cells (Fig. 4 B). This suggests that the transition of a subset of intratumoral LAG3⁻tdT⁺ cells into peripheral LAG3⁻tdT⁺ cells occurs prior to d19, while maintaining a shared lineage origin. In addition, the Venn diagram illustrates the overlap of specific accessible chromatin regions (ACRs) among the three subsets. At d19, intratumoral LAG3⁻tdT⁺ cells shared ∼80% of their ACRs with intratumoral LAG3⁺tdT⁺ cells, whereas they only shared ∼50% of ACRs with LAG3⁻tdT⁺ cells in the DLNs (Fig. 4 C).

We then evaluated transcription start site (TSS)-centered ATACseq signal profiles to assess chromatin accessibility across different subsets (Fig. 4 D), enabling comparison of promoter accessibility and overall regulatory landscapes between tumor- and LN-derived populations. All groups showed clear enrichment of accessibility around the TSS, with stronger signals in intratumoral LAG3⁻tdT⁺ cells and distinct patterns in LAG3⁺tdT⁺ cells, reflecting context-dependent chromatin remodeling. These findings highlight differential regulatory activity that may underlie functional differences between subsets and warrant further investigation of transcription factor motifs and gene programs driving these accessibility changes. To further evaluate the regulatory programs associated with chromatin accessibility changes, we examined the expression of key transcription factor–associated gene signatures across different tdT⁺ subsets. In peripheral LAG3⁻tdT⁺ cells, transcriptional programs associated with effector survival, including *Stat4*- and *Stat5*-related genes, appeared more predominant. The stem-like program driven by forkhead box O1 (*Foxo1*) also showed stronger activity, whereas signatures associated with exhaustion remained minimal. In contrast, intratumoral LAG3⁺tdT⁺ cells exhibited strong engagement of exhaustion programs along with TGF-β–associated signaling, as reflected by elevated SMAD family member 2 and 3 (*Smad2* and *Smad3*)-associated accessibility. Intratumoral LAG3⁻tdT⁺ cells at this late time point also displayed a more exhausted phenotype compared with peripheral LAG3⁻tdT⁺ cells (Fig. 4 E).

Reinforcing these observations, we performed a joint principal component analysis (PCA) integrating our tdT⁺ populations with publicly available reference datasets (GSE86797) (Huang et al., 2025) representing naive, effector, memory, and exhausted CD8⁺ T cells derived from an LCMV clone 13 infection model. Based on Euclidean distance in PC space, intratumoral LAG3⁺tdT⁺ cells were closest to the exhausted state, whereas intratumoral LAG3⁻tdT⁺ cells and peripheral LAG3⁻tdT⁺ cells aligned more closely with memory and naive populations (Fig. 4 F). Comparison of ATACseq chromatin accessibility tracks at the *Pdcd1* and *Tox* loci revealed accessible peaks in tumoral and peripheral LAG3⁻tdT⁺ cells that were synonymous with T_{EX} cells in LCMV clone 13 (Fig. S3 G) (Huang et al., 2025). Of particular note is the −23.8 kb enhancer in *Pdcd1* that is exclusively accessible in T_{EX}, but not naive, memory or effector T cells in LCMV clone 13, which also seems to be accessible in tumoral and peripheral LAG3⁻tdT⁺, albeit to a lesser extent in the latter. Consistent with these epigenetic patterns, flow cytometry at d19 revealed a low frequency of memory precursor effector cells and an absence of central memory T cells (T_{CM}) within LAG3⁺tdT⁺ CD8⁺ T cells, whereas peripheral LAG3⁻tdT⁺ CD8⁺ cells were enriched for both subsets (Fig. 4 G).

Taken together, ATACseq and flow cytometry analyses indicate that despite sharing a common TCR lineage, intratumoral LAG3⁺tdT⁺ and LAG3⁻tdT⁺ CD8⁺ T cell exhibit exhaustion-associated epigenetic and effector features, whereas peripheral LAG3⁻tdT⁺ CD8⁺ cells acquire memory-associated chromatin accessibility and effector–memory phenotypes during tumor progression.

Progenitor LAG3⁻tdT⁺ CD8⁺ T_{EX} cells persist in the periphery and contribute to anti-tumor immunity

We next asked whether LAG3⁻tdT⁺ CD8⁺ T cells in the periphery, that exhibited a progenitor T_{EX} phenotype, had any functional role in tumor-specific immunity, similar to LN-resident stem-like CD8⁺ T_{EX} cells (Connolly et al., 2021; Huang et al., 2022). Primary B16-F10 tumors were resected on d12, mice rested for 30 days, and then rechallenged with B16-F10 cells on the contralateral side to the primary tumor (Fig. 5 A).

Compared with sham control, which were injected with PBS instead of B16-F10 tumor followed by d8–10 tamoxifen treatment, tumor-resected mice had significantly more tdT⁺ cells in the secondary tumor compared with the periphery, indicative of an antigen-mediated recall response (Fig. 5 B). Analysis of the CD8⁺ T cell compartment showed that 10% of TILs were LAG3⁺tdT⁺ and 10% were LAG3⁻tdT⁺ CD8⁺ T_{EX} cells. LAG3⁺tdT⁺ CD8⁺ T_{EX} cells from the secondary rechallenge were restricted to the TME, whereas LAG3⁻tdT⁺ CD8⁺ T_{EX} cells were in both the TME and periphery (Fig. 5 C). Based on tamoxifen labeling, LAG3⁺tdT⁺ CD8⁺ T_{EX} cells in the secondary tumor could only be derived from LAG3⁻tdT⁺ cells that were generated during the primary tumor phase (i.e., d8–10 after initial tumor inoculation) and persisted in the periphery over the 30-day resting phase. Indeed, these cells were the only tdT⁺ population in peripheral blood of tumor-resected mice before rechallenge on d42 (Fig. S4 A). Additional experiments using dual tumor inoculation confirmed that this expansion was antigen-driven rather than nonspecific, as robust accumulation of LAG3⁺tdT⁺ cells occurred only in antigen-matched tumors (B16-F10), whereas unrelated tumors (MC38) showed minimal expansion (Fig. S4, B–G). Thus, LAG3⁻tdT⁺ CD8⁺ T_{EX} cells were capable of persistence and self-renewal in the absence of antigen as well as differentiation upon antigen restimulation.

CD8⁺ TILs and lymphocytes in the periphery were evaluated for IR expression (Fig. 5 D and Fig. S5 A). LAG3⁺tdT⁺ CD8⁺ T_{EX} cells co-expressed high levels of PD1, TIM3, and TIGIT, whereas LAG3⁻tdT⁺ CD8⁺ T_{EX} cells had relatively low co-expression of these IRs. We also investigated the exhaustion state of tdT⁺ subsets from rechallenged tumors. Intratumoral LAG3⁺tdT⁺ and LAG3⁻tdT⁺ subsets were dominant in intermediate and terminal T_{EX} cells (Fig. 5, E and F). TIM3 expression was also observed in the peripheral LAG3⁻tdT⁺ compartment, where these cells retained a more progenitor exhausted phenotype (Fig. S5 B), suggesting that peripheral LAG3⁻tdT⁺ CD8⁺ T_{EX} cells further gave rise to more terminally T_{EX} cells upon antigenic restimulation. In addition, LAG3⁺tdT⁺ and LAG3⁻tdT⁺ CD8⁺ T_{EX} cells

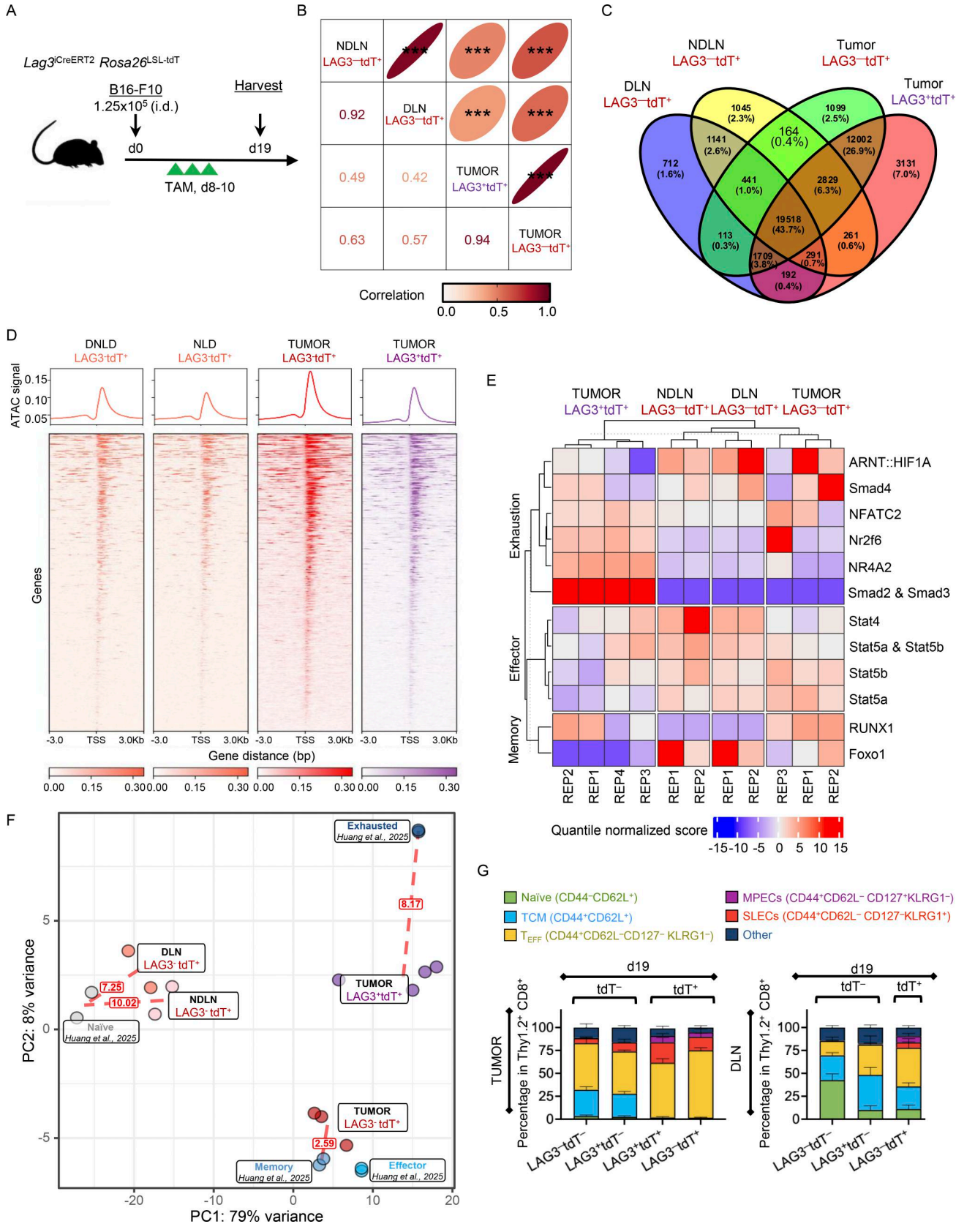

Figure 4. **Epigenetic and functional divergence of intratumoral and peripheral tdT⁺ cells. (A)** Experimental strategy for analysis of chromatin accessibility between different tdT CD8⁺ T cell subsets. B16-F10 tumor implanted in *Lag3*^{iCreERT2} *Rosa26*$^{LSL\text{-}tdT}$ mice, treated with three tamoxifen injections (2 mg in 5% EtOH/sunflower oil) at d8–10, and assessed for chromatin accessibility on d19. Lymphocytes were isolated from NDLNs and DLNs, and intratumoral LAG3⁻tdT⁻, LAG3⁺tdT⁺, and LAG3⁻tdT⁺ CD8⁺ T cell subsets were flow-sorted and subjected to ATACseq. **(B)** Pairwise correlations among tdT⁺ CD8⁺ T cell subsets isolated

from NDLNs, DLNs, and tumors, determined by Pearson correlation analysis. Shapes represent correlation values, as indicated by the corresponding numbers in the all-by-all matrix. Correlations approaching 1 are depicted as elongated lines, whereas correlations closer to zero resemble circles. The color bar indicates correlation values, with red indicating positive correlation. **(C)** Venn diagram showing overlap of high variable peaks among tdT⁺ CD8⁺ T cell subsets. **(D)** Heatmaps with aggregate profiles of chromatin accessibility centered on TSSs across indicated subsets. **(E)** Heatmap of representative transcription factors associated with exhaustion, effector, and memory programs, showing quantile-normalized expression scores across subsets. **(F)** Joint PCA of ATACseq data from tdT⁺ CD8⁺ T cell subsets and reference differentiation states (naive, effector, memory, and exhausted). Different tdT⁺ populations include LAG3⁻tdT⁺ of NDLNs (pink), LAG3⁻tdT⁺ of DLNs (coral), intratumoral LAG3⁻tdT⁺ (red), and intratumoral LAG3⁺tdT⁺ (purple). Reference states are shown in shades of blue/grey. Red lines indicate the closest reference state with Euclidean distance values. **(G)** Phylum plot represents the percentage of T_{naive} (green), T_{CM} (blue), T_{EFF} (yellow), MPECs (magenta), SLECs (red), and other (dark blue) immune cell subsets in both tumor and DLNs across different tdT subsets. *n* = 5 mice, pooled from two independent experiments. Data in B–F are representative of two independent experiments. ***P < 0.001 by Pearson correlation coefficient (B). Error bars represent mean ± SEM.

from the secondary tumor had a more terminal T_{EX} phenotype compared with the primary tumor.

To understand the functionality of periphery-derived LAG3⁻tdT⁺ CD8⁺ T_{EX} cells that persisted ≥30 days compared with those from primary tumor-bearing mice on d11 before resection, we evaluated CD44⁺tdT⁺ T_{EX} cells from the periphery of mice that remained tumor-free for 48 days after primary tumor resection on d12 (d60). We mapped the expression profile of these periphery-derived CD44⁺tdT⁺ T_{EX} cells on d60 to the clusters C1–15 identified by scRNAseq. Memory-like features were already induced by d11, as evidenced by enrichment of *Slamf6*⁺ progenitor-memory (C10) and memory precursor (C8) signatures. On d60, these memory traits within CD44⁺tdT⁺ cells were also present albeit in a lower frequency. Instead, the peripheral CD44⁺tdT⁺ cells at this late time point were predominated by a more "differentiated" central memory–associated phenotype (C4) that is consistent with a stress-adapted, long-lived circulating T_{CM} signature previously reported in LCMV-infected host (Angelosanto et al., 2012; Kurd et al., 2020) (Fig. S3 C and Fig. 5 G). Taken together, transcriptome analyses suggested that progenitor LAG3⁻tdT⁺ T_{EX} cells can persist long-term and contribute to the tumor-specific memory pool.

Finally, to determine whether peripheral LAG3⁻tdT⁺ T_{EX} cells contribute functionally to tumor control, we next assessed tumor growth following their selective depletion. We used *Lag3*^{iCreERT2}*Rosa26*$^{LSL\text{-}tdT}$*Rosa26*$^{LSL\text{-}DTR}$ mice in which tdT⁺DTR⁺ cells can be conditionally ablated upon administration of diphtherial toxin (DTX) (Fig. 5 H). To validate the efficiency of peripheral LAG3⁻tdT⁺ T_{EX} cell depletion following secondary rechallenge, we examined both DLNs and NDLNs and observed a reduction in LAG3⁻tdT⁺ T_{EX} cell frequency upon diphtheria toxin treatment. Although their baseline abundance was low, a reduced number was observed (Fig. S5 C). Strikingly, this depletion led to significantly accelerated growth of the secondary tumor and thus abrogation of the anti-tumor memory response, demonstrating that peripheral LAG3⁻tdT⁺ T_{EX} cell play a critical role in sustaining effective memory recall (Fig. 5 I). These results suggest that even a relatively small population of peripheral LAG3⁻tdT⁺ T_{EX} cell can contribute substantially to anti-tumor immunity.

Discussion

Delineating the functional heterogeneity and plasticity of T_{EX} cells is important to understand tumor-induced T cell dysfunction. In this study, we used a unique *Lag3*-lineage tracing tool, *Lag3*^{iCreERT2}*Rosa26*$^{LSL\text{-}tdT}$ mice, to characterize the developmental trajectories and functional properties of *Lag3*-expressing T_{EX} cells. Following tamoxifen exposure, Cre-mediated recombination irreversibly activates tdT expression, thereby permanently labeling cells with a history of *Lag3* expression. Importantly, tdT labeling reflects prior *Lag3* expression at the time of tamoxifen induction and is not dependent on sustained expression thereafter. Our data illustrate the following three key observations.

First, we identified two distinct subsets: surface LAG3-expressing T_{EX} cells (LAG3⁺tdT⁺ cells) and a unique population of LAG3⁻tdT⁺ cells that lack surface LAG3 expression. LAG3⁺tdT⁺ CD8⁺ T_{EX} cells were restricted to the TME, whereas LAG3⁻tdT⁺ CD8⁺ T_{EX} cells were found in both the tumor and the periphery. While both tdT⁺ populations coexist in the TME, their relative predominance differed as demonstrated across different tumor models with diverse immunogenicity and immunotherapy sensitivity. The current study does not determine which subset contributes to ICB response, and further investigation is needed to understand the functionality of these tdT⁺ cells in immunogenic versus non-immunogenic tumors. TCR analysis revealed that, as the tumor progresses, all clones of intratumoral LAG3⁻tdT⁺ cells are shared with intratumoral LAG3⁺tdT⁺ and peripheral LAG3⁻tdT⁺ cells. Peripheral LAG3⁻tdT⁺ cells also share a substantial number of clonotypes with intratumoral LAG3⁺tdT⁺ cells only at the late time point. These findings suggest a developmental linkage among these populations and, notably, indicate that LAG3⁺tdT⁺ cells, upon losing surface LAG3, have the potential to migrate to the periphery. Consistent with these observations, intratumoral adoptive transfer of LAG3⁺tdT⁺ CD8⁺ T cells gave rise to LAG3⁻tdT⁺ cells within the tumor that subsequently migrate into the periphery. LAG3⁻tdT⁺ cells were detected in the DLNs and NDLNs in a subset of recipients, with the limited frequency likely reflecting the low number of transferred cells. In addition, tetramer staining and pMEL dual-tumor validation experiments further confirmed that LAG3⁻tdT⁺ cells are tumor-antigen reactive. Collectively, these findings support a lineage relationship between LAG3⁺tdT⁺ and LAG3⁻tdT⁺ CD8⁺ T cells and validate the fidelity of the *Lag3* lineage–tracing strategy. Notably, although Adam10-mediated shedding is a mechanism regulating surface LAG3 expression (Andrews et al., 2020), our data suggest that this process is unlikely to account for the loss of LAG3 in LAG3⁻tdT⁺ cells. The combination of substantial *Adam10* expression and the absence of detectable *Lag3* transcripts indicate that the loss of LAG3 expression is not due to ADAM10-mediated posttranslational shedding. Instead,

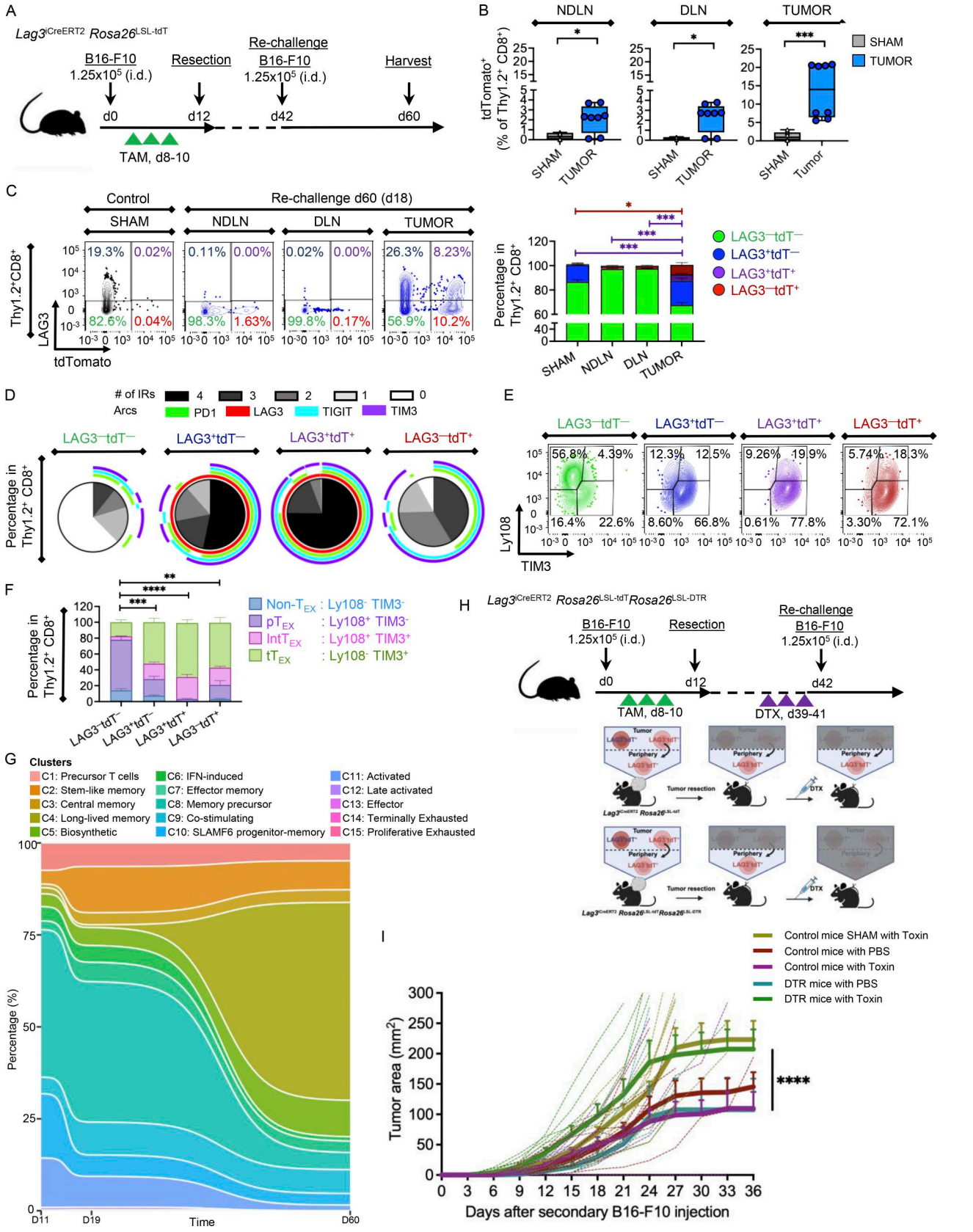

Figure 5. **Lag3−tdT+ CD8+ T_{EX} stem cell–like progenitor cells persist in circulation and contribute to anti-tumor immunity. (A)** Scheme to evaluate differentiation potential of LAG3−tdT+ CD8+ T cells in circulation upon tumor rechallenge. *Lag3*iCreERT2 *Rosa26*LSL-tdT mice were i.d. injected with B16-F10 cells (1.25×10^5), treated with three tamoxifen injections (2 mg in 5% EtOH/sunflower oil) at d8–10, and tumor was resected on d12. After a 30-day resting phase,

mice were rechallenged on d42 with i.d. injection of B16-F10 cells (1.25×10^5), and tumors were harvested 18 days after rechallenge. SHAM controls were injected with 1× PBS on d0 but followed a similar regime. **(B)** tdT expression was assessed on Thy1.2$^+$ CD8$^+$ T cells in NDLNs, DLNs, and tumor isolated from A for SHAM control (grey) and tumor-bearing (blue) mice. **(C)** LAG3 and tdT expression on CD8$^+$ T cells isolated from A. Phylum plot represents the percentage of tdT subsets in SHAM, NDLNs, DLNs, and tumor. **(D)** Spice plot visualization of IR co-expression (n = 4) on tdT subsets from A. **(E)** LY108 and TIM3 expression assessed on tdT subsets from A. **(F)** Phylum plot represents the percentage of LY108$^-$TIM3$^-$ (blue), LY108$^+$TIM3$^-$ (purple), LY108$^+$TIM3$^+$ (pink), and LY108$^-$TIM3$^+$ (green) in tdT subsets. **(G)** CD44$^+$tdT$^+$ cells from scRNAseq on d11, d19, and d60 were analyzed for functional enrichment of 15 clusters (C1–C15). **(H)** Scheme to assess tumor growth after depletion of peripheral LAG3$^-$tdT$^+$ CD8$^+$ T cells persisting in the system. 300 ng of diphtherial toxin was treated on d39–41. **(I)** Tumor growth curves across five different groups. Yellow: *Lag3*^{iCreERT2} *Rosa26*$^{LSL\text{-}tdT}$ mice received PBS instead of primary tumor on d0 and were treat with DTX on d39–41 (n = 10); red: *Lag3*^{iCreERT2} *Rosa26*$^{LSL\text{-}tdT}$ mice received primary tumor and were treat with PBS instead of DTX on d39–41 (n = 10); purple: *Lag3*^{iCreERT2} *Rosa26*$^{LSL\text{-}tdT}$ mice received primary tumor and were treat with DTX on d39–41 (n = 11); blue: *Lag3*^{iCreERT2} *Rosa26*$^{LSL\text{-}tdT}$ *Rosa26*$^{LSL\text{-}DTR}$ mice received primary tumor and were treat with PBS instead of DTX on d39–41 (n = 6); green: *Lag3*^{iCreERT2} *Rosa26*$^{LSL\text{-}tdT}$ *Rosa26*$^{LSL\text{-}DTR}$ mice received primary tumor and were treat with DTX on d39–41 (n = 10). Results in I are representative of three independent experiments, with the indicated n per group. Data in B–F are pooled from three independent experiments with n = 8 mice per group. Data in G are representative of two independent experiments. *P < 0.05; **P < 0.01; ***P < 0.001; ****P < 0.0001; ns, not significant, by unpaired t test (B), two-way ANOVA (C and F), or mixed-effect analysis (I). Error bars represent mean ± SEM.

transcriptional downregulation likely underlies the generation of LAG3$^-$tdT$^+$ cells, although the mechanisms driving this transition remain to be elucidated.

Despite the overall fidelity of the model, several limitations should be considered. The timing of tamoxifen treatment can influence the relative proportions of tdT$^+$ subsets observed at later time points; for example, we observed an apparent drop in tdT$^+$ cells in the d13–15 treatment group. This may reflect biological factors, such as an influx of bystander cells recruited by inflammation and chemokine signaling, or reduced tamoxifen penetration in larger tumors at later stages. In addition, CD8$^+$ T cells may vary in their sensitivity to tamoxifen depending on their activation state, which could influence labeling efficiency and represents another caveat of the model. Finally, low level background labeling likely reflects basal Cre activity, which may in part result from tonic activation of microbiota reactive T cells at mucosal sites (Honda and Littman, 2016; Yang and Cong, 2021).

Second, chromatin profiling revealed that intratumoral LAG3$^-$tdT$^+$ and LAG3$^+$tdT$^+$ cells shared similar accessible regions, whereas peripheral LAG3$^-$tdT$^+$ cells displayed distinct features at late time points. As tumors progressed, LAG3$^-$tdT$^+$ cells exhibited characteristics of progenitor exhausted cells and appeared to follow two potential trajectories: one subset migrated to the periphery and acquired a stem-like memory-like phenotype, while the remaining cells that persisted within the TME became progressively more terminally exhausted, resembling LAG3$^+$tdT$^+$ cells. RNA velocity analysis further indicated that this migratory transition was largely complete by the late time point, in agreement with prior studies showing that the epigenetic landscape of T_{EX} cells is relatively stable once established within the TME (Abdel-Hakeem et al., 2021; Pauken et al., 2016; Yates et al., 2021). Together, these findings highlight the critical role of both spatial and temporal cues in shaping the fate of tdT$^+$ cells.

Third, phenotypic and transcriptomic analyses suggested clear functional differences between the subsets. Importantly, peripheral LAG3$^-$tdT$^+$ cells demonstrated the capacity to persist long-term outside the tumor and retain the capacity to generate terminal T_{EX} upon antigen re-encounter, thereby contributing to the memory pool. Functionally, depletion of peripheral LAG3$^-$tdT$^+$ cells resulted in accelerated tumor growth, reflecting their role in sustaining anti-tumor immunity. Taken together, consistent with the substantial developmental and functional heterogeneity of T_{EX} in tumor (Beltra et al., 2020; Hudson et al., 2019; Zhou et al., 2023), peripheral LAG3$^-$tdT$^+$ T_{EX} cells represent a progenitor-like subset with greater plasticity that supports durable immune responses, in contrast to the more terminally exhausted LAG3$^+$tdT$^+$ cells.

In summary, our data suggest that *Lag3*$^+$ subsets play disparate roles in shaping tumor-associated CD8$^+$ T_{EX}. *Lag3* transcriptional activation coincides with epigenetic imprinting of T_{EX} that is stable both temporally and spatially. Thus, future investigation of the environmental signals that drive *Lag3* transcription in CD8$^+$ T cells is warranted. While membrane LAG3 expression helps shape T_{EX} functionality by driving tumor retention and terminal exhaustion, LAG3$^-$tdT$^+$ T_{EX} cells retain substantial functionality and contribute to tumor-specific memory. Therefore, our results support the rationale for antibody-based therapeutic targeting of LAG3$^+$ T_{EX} cells to unleash anti-tumor immunity.

Materials and methods

Mice

Rosa26$^{LSL\text{-}tdTomato}$, C57BL/6, pMEL, *Rag1*$^{-/-}$, and CD45.1 and mice were obtained from The Jackson Laboratory. All animal experiments were performed in the American Association for the Accreditation of Laboratory Animal Care–accredited, specific pathogen–free facilities in Division of Laboratory Animal Resources, University of Pittsburgh School of Medicine. Female and male mice were used. Mice were used for studies when 4–5 wk old. Animal protocols were approved by the Institutional Animal Care and Use Committees of University of Pittsburgh.

Generation of *Lag3*^{iCreERT2} *Rosa26*$^{LSL\text{-}tdTomato}$ mice

Tamoxifen-inducible *Lag3*^{iCreERT2} transgenic mice were generated by inserting the iCreERT2 cassette downstream of the *Lag3* promoter and the Kozak start site. The DNA was dialyzed and microinjected into C57BL/6 zygotes and the resulting pups were genotyped. *Lag3*^{iCreERT2} mice were then crossed to *Rosa26*$^{LSL\text{-}tdTomato}$ mice to generate the *Lag3*^{iCreERT2} *Rosa26*$^{LSL\text{-}tdTomato}$ line (Fig. 1 A). *Rosa26*$^{LSL\text{-}tdTomato}$ mice have a *loxP*-flanked STOP cassette, which prevents transcription of the red fluorescent

protein tdTomato, upon Cre recombinase STOP cassette is deleted, resulting in tdTomato fluorescence. This murine model allows for selectively fate mapping LAG3$^+$ T cells following tamoxifen induced Cre recombination.

Cell lines and reagents

Melanoma cell lines B16-F10, B16-gp100, YUMM1.7, and YUMMER1.7 and colon adenocarcinoma cells MC38 were used in this study. B16-F10 cells were received from Mary J. Turk (Dartmouth College, Hanover, NH, USA). B16-gp100 cells were received from Paul M. Sondel (University of Wisconsin, Madison, WI, USA). YUMM1.7 and YUMMER1.7 cells were received from Marcus W. Bosenberg (Yale University, New Haven, CT, USA). MC38 were received from James P. Allison (M.D. Anderson Cancer Center, Houston, TX, USA). B16-F10 and B16-gp100 cells were cultured in complete Roswell Park Memorial Institute medium-1640 (cRPMI-1640; Lonza); supplemented with 10% FBS, 2 mM glutamine, 5 mM HEPES, 1 mM pyruvate, 100 µM nonessential amino acids, penicillin (100 U/ml), streptomycin (100 µg/ml), and 2-mercaptoethanol (2-ME). B16-gp100 cells were cultured in complete RPMI-1640 with the addition of Geneticin (0.8 mg/ml; Thermo Fisher Scientific). YUMM1.7 and YUMMER1.7 were cultured in complete DMEM/F12 (cDMEM/F12) supplemented with 10% FBS, penicillin (100 U/ml), streptomycin (100 µg/ml), and 1% nonessential amino acids (100×). MC38 cells were cultured in cDMEM (Lonza); supplemented with 10% FBS, 2 mM glutamine, 5 mM HEPES, 1 mM pyruvate, 100 µM nonessential amino acids, penicillin (100 U/ml), streptomycin (100 µg/ml), and 2-ME. All cells were cultured at 37°C and 5% CO_2.

Tumor models

Mice were injected with B16-F10 (1.25×10^5 cells, i.d.), B16-gp100 melanoma (1.25×10^5 cells, i.d.), YUMM1.7 (1.25×10^5 cells, i.d.), or YUMM1.7 (1.00×10^5 cells, s.c.), YUMMER1.7 (1.25×10^5 cells, i.d.), and MC38 (5.00×10^5 cells, s.c.). NDLNs and DLNs and tumors were harvested for analysis at the defined time points as indicated.

Surgical tumor excision and rechallenge

Surgical excision of primary tumors was performed as previously described (Liu et al., 2020). Briefly, the i.d. primary B16-F10 tumors implanted in the right flank were excised on d12. Mice were anesthetized with isoflurane, and tumors were surgically removed with a 2-mm perimeter of healthy skin under aseptic conditions. Steel wound clips were used for incision closure. Mice were given rimadyl tablet, for 3 days, from 24 h before, day of surgery, and after surgery for pain management. After 30-days resting period, mice were rechallenged with B16-F10 melanoma cells (1.25×10^5 cells, i.d.) in the left flank and harvested for analysis at the defined time points as indicated.

Intratumoral adoptive transfer of LAG3$^+$tdT$^+$ CD8$^+$ T cells

LAG3$^+$tdT$^+$ CD8$^+$ T cells were isolated from d11 B16-F10 tumors of *Lag3*^{iCreERT2} *Rosa26*$^{LSL\text{-}tdT}$ donor mice (Thy1.2$^+$ CD45.2$^+$), which received tamoxifen on d8–10. Single-cell suspensions were prepared from tumors, and cells were enriched and sorted by flow cytometry based on singlets, viability, Thy1.2 expression, CD8 expression, tdT positivity, and LAG3 expression. Sorted cells were collected as donor populations for adoptive transfer. For intratumoral adoptive transfer, $3–4 \times 10^3$ cells LAG3$^+$tdT$^+$ CD8$^+$ T cells (CD45.2$^+$) in 50 µl sterile PBS were injected into d7 B16-F10 tumors of CD45.1$^+$ recipients. Tumors and DLNs were harvested at d12 for analysis.

Adoptive transfer of pMEL cells

CD8$^+$ T cells were negatively selected from spleen and LNs of *Lag3*^{iCreERT2} *Rosa26*$^{LSL\text{-}tdT}$ pMEL mice by incubation with a biotin-conjugated antibody cocktail (anti-CD4, CD19, B220, CD11b, CD11c, CD25, I-Ab, CD49b, CD105, CD16/32, γδTCR, Ly6G/C, and Ter119) on ice for 20 min. Cells were then washed and incubated with Pierce Streptavidin Magnetic beads (Thermo Fisher Scientific) on ice for 15 min. Cells were placed on a magnet, and non-bound cells were extracted resulting in CD8$^+$ T cells with >90% purity. C57BL/6 mice received a prophylactic adoptive transfer of purified pMEL cells on the indicated day (day −1 [d−1]), followed by the tumor administration with B16-gp100 melanoma cells after 24 h (1.25×10^5 cells, i.d.). NDLNs and DLNs and tumors were harvested for analysis at the defined time points as indicated.

Tamoxifen administration

Mice were randomized and either received three consecutive intraperitoneal injections of tamoxifen (Thermo Fisher Scientific; 2 mg in 5% EtOH/sunflower oil) or vehicle as a control. Tissues (tumor, spleen, and LNs) were harvested for analysis at the defined time points.

Diphtheria toxin administration

Mice were randomized and either received three consecutive intraperitoneal injections of diphtheria toxin (List Labs; 300 ng/mouse) or vehicle (PBS) as a control.

Single-cell isolation

For isolation of TILs, mice injected with B16-F10, B16-gp100, YUMM1.7, YUMMER1.7, and MC38 tumors were dissected, and tumor, NDLN, and DLN were collected for analysis on the indicated time point. TILs were isolated with enzymatic digestion cocktail containing collagenase IV (Worthington Biochemical, 1 mg/ml), dispase (STEMCELL Technologies, 1 mg/ml), and DNase (5 mg/ml), followed by mechanical disruption and incubation at 37°C for 30 min. After incubation, cells were processed for red blood cell lysis to obtain single-cell suspension. For isolation of lymphocytes from NDLN and DLN, LNs were processed directly from live/dead staining after single-cell suspension.

Antibodies and flow cytometry

Live/dead cell discrimination was performed on the lymphocytes from tumor, NDLN, and DLN by staining with Ghost Viability Dye (Tonbo Biosciences) in 1× PBS at 4°C for 15 min. Fc block was performed to avoid nonspecific binding by staining with anti-CD16/32 at 4°C for 15 min. Surface staining was performed in FACS staining buffer (0.5% sodium azide/1× PBS/5% FBS) containing the designated antibody cocktails at 4°C for

30 min. For surface staining, single-cell suspensions were stained with antibodies against Thy1.2 (30-H12; BioLegend), Thy1.1 (OX-7; BD), CD44 (IM7; BioLegend), CD4 (RM4-5; Invitrogen), CD8α (53-6.7; Invitrogen), TIM3 (5D12; BD), Tigit (GIG07; Invitrogen), Ly108 (13G3; BD), Tcf1 (C63D9; Cell Signaling), Tox (REA473; Miltenyi Biotec), PD1 (RMP1-30; BioLegend), Foxp3 (FJK-16 s; Invitrogen), CD62L (MEL-14; BioLegend), Klrg1 (2F1; BD), CD127 (A7R34; BioLegend), and LAG3 (4-10-C9).

For transcription factors, Foxp3, TCF1, and TOX cells were fixed and permeabilized using the Fix/Perm buffer (eBioscience) at 4°C for at least 30 min. Cells were subjected to two independent washing cycles in 1× Perm buffer. For intracellular staining, cells were stained with antibody cocktail at 4°C for 30 min. Cells were analyzed on Fortessa (BD Biosciences), and data analysis was performed using FlowJo v. 10.10 (Tree Star).

For $CD8^+$ T cells negative selection, biotin-conjugated antibodies against the following targets were used: CD4 (RM4-5; BioLegend), CD19 (6D5; BioLegend), B220 (RA3-6B2; eBioscience), CD11b (M1/70; BioLegend), CD11c (N418; BioLegend), CD25 (PC61; BioLegend), I-Ab (KH74; BioLegend), CD49b (DX5; eBioscience), CD105 (MJ7/18; BioLegend), CD16/32 (93; Invitrogen), γδTCR (eBioGL3; Invitrogen), Ly-6g/c (RB6-8C5; BioLegend), and Ter119 (TER119; BioLegend).

scRNAseq and TCRseq

Single-cell transcriptome profiling was performed using the 10X Genomics Chromium drop-seq platform (V1 chemistry). *Lag3*^{iCreERT2} *Rosa26*$^{LSL\text{-}tdT}$ mice (male, 4–5 wk of age) implanted with B16-F10 tumors were used for scRNAseq. Tumor and LNs were harvested on d11 and d19, and sample multiplexing was performed using CITEseq. To achieve this, samples were stained with TotalSeq-C anti-mouse hashtag antibodies along with the surface antibody cocktail at 4°C for 30 min, followed by washing with FSB buffer (1× PBS/10% FBS). The lymphocytes from tumor and LNs were freshly sorted, stained with uniquely barcoded TotalSeq-C antibodies for $LAG3^-tdT^-$, $LAG3^+tdT^+$, and $LAG3^-tdT^+$ $CD8^+$ T cells, and resuspended in 1× PBS containing 0.04% bovine serum albumin (BSA, Sigma-Aldrich). Libraries were created immediately following isolation of sorted cells. Sorted cells were loaded into 10X controller for droplet generation targeting a recovery of precisely 2,500 cells per sample. After droplet partitioning, cells were lysed and mixed with reverse transcribed followed by the Dynabead cDNAs clean up and amplification (14 cycles). Amplified cDNAs were then sheared, repaired, and A-tailed, and adaptors were ligated. The library concentration was then quantified using KAPA Universal Library Quantification Kit (KK4824). The libraries were further checked for the amplified cDNA length on a Bioanalyzer using a High Sensitivity DNA kit.

Following generation and quantification of single-cell libraries, samples were pooled and diluted to 2 nM for downstream sequencing. Sequencing libraries were loaded on Illumina, NovaSeq 6000 at the UPMC Genome Center. Samples were sequenced using NovaSeq 6000 S1 v1.5 kits (150 cycles) with the following parameters: for v1 chemistry—read 1: 26 cycles, i7 index: 8 cycles, and read 2: 90 cycles.

Bulk-ATACseq

Lag3^{iCreERT2} *Rosa26*$^{LSL\text{-}tdT}$ mice (male, 4–5 wk of age) implanted with B16-F10 tumors were used for ATAC-RNAseq. Tumor and LNs were harvested on d19. To achieve this, samples were stained with the surface antibody cocktail at 4°C for 30 min, followed by washing with FSB buffer (1× PBS/10% FBS). The lymphocytes from tumor, NDLN, and DLN were freshly sorted for $LAG3^-tdT^-$, $LAG3^+tdT^+$, and $LAG3^-tdT^+$ $CD8^+$ T cells and resuspended in 1× PBS containing 0.04% bovine serum albumin (BSA, Sigma-Aldrich) and counted using Cellometer Auto2000 (Nexcelom). Sequencing libraries were prepared using the Nextera PCR primer NS500 kit (Illumina) and then quantitated using the cHSD1000 kit. The samples were pooled in equal concentrations and sequenced on the Ilumina NextSeq500 with 2 × 75 paired end reads.

Demultiplexing, alignment, and generation of gene/barcode matrices

The process began with demultiplexing and aligning sequenced samples, generating gene/barcode matrices through the Cell Ranger software (10X Genomics version 6.1.1) preprocessing pipeline. Illumina BCL files were converted to FASTQs via mkfastq pipeline, aligned with the mouse genome refdata-gex-mm10-2020-A as a reference, and used to obtain gene/barcode matrices. Subsequently, the Seurat R package was employed for analysis. Exclusion criteria were set for cells with fewer than 300 detected genes or mitochondrial genes per cell accounting for <20%. Counts were demultiplexed and normalized using Seurat's built-in functions (NormalizeData and HTODemux) with default parameters to remove doublets.

Batch effects were addressed using the harmony (Korsunsky et al., 2019) package, integrating and preprocessing datasets within Seurat's (Hao et al., 2024) standard workflow. The dimensional reduction output from harmony was then utilized for data visualization through Seurat's built-in function RunUMAP. Louvain clustering, based on the top 35 harmony principal components with a resolution set to 0.8, was set for using Seurat's FindClusters. Clusters with cell numbers <100 and situated away from the primary UMAP were considered noise signals and trimmed off. As a result, 50,272 cells were retained for downstream analysis.

The cluster annotation was performed relying on the top ranked significantly expressed genes calculated by R package presto, and marker genes were identified with cosine similarity-based method from R package COSG. According to the expression status of gene group in each cluster, and refer to other previous analysis literature, cluster annotation was conducted.

RNA velocity

Cell developmental pseudotime directionality was assessed through RNA velocity, exploiting the identification of spliced and unspliced transcripts. The analysis was executed using the velocyto package (v0.17) in Python, handling CellRanger count files. The subsequent analysis followed the scVelo pipeline (v0.2.4) for result analysis and visualization. To outline the process, all .loom files from the velocyto alignment were merged with the barcode-adjusted dataset. The merged data underwent

a series of steps, including filtering, normalization, and projection onto the UMAP distribution derived from the Seurat project.

scTCRseq analysis

Following the demultiplexing process via mkfastq, the sequenced TCR file underwent a rigorous alignment procedure. This alignment was specifically performed against the refdata-cellranger-vdj-GRCm38-alts-ensembl-5.0.0 reference genome. The alignment process was meticulously executed by utilizing the vdj pipeline embedded within the cellranger software. Additionally, to enhance the TCR repertoire profiling of the corresponding samples, an advanced tool called TRST4 was deployed. This tool leveraged gene expression fastq files to predict and expand the intricate details of the TCR repertoire. This step involved a thorough analysis of the gene expression patterns, contributing to a more comprehensive understanding of the TCR landscape.

The outputs generated by both platforms, encompassing the aligned TCR files from cellranger and the expanded TCR repertoire predictions from TRUST4 (Song et al., 2021), were collected and pooled. This pooling laid the groundwork for subsequent in-depth analyses and insights into the TCR dynamics within the biological samples under examination. TCR cdr3 from particular days were collected to evaluate their share relationship among different conditions and visualized with R package circlize (Gu et al., 2014).

ATACseq downstream analysis

The processing of raw ATACseq FASTQ files, obtained from paired-end sequencing, were processed using the script available at repository (https://github.com/wherrylab/jogiles_ATAC). The samples were aligned to the GRCm38/mm10 reference genome using the Bowtie2 algorithm. Subsequently, Samtools was utilized to eliminate unmapped, unpaired, and mitochondrial reads. To ensure the integrity of the data, ENCODE blacklist regions were removed from the aligned samples (https://github.com/Boyle-Lab/Blacklist). PCR duplicates were removed using Picard.

Peak calling was performed using MACS2 v2, with a false discovery rate q value set at 0.01. For each experiment, a union peak list was generated by combining peaks from all samples, and merged overlapping peaks were merged using bedtools merge. The number of reads within each peak was determined using bedtools coverage.

Batch correction and visualization. Raw gene-level count matrices were corrected for batch effects using ComBat-seq (R package sva [Zhang et al., 2020]), which preserves integer counts for downstream modeling. Signal heatmaps were generated with deepTools using computeMatrix to build the signal matrix and plotHeatmap for rendering with default parameters.

Joint PCA was performed by integrating tdT$^+$ populations with reference datasets (GSE86797) (Huang et al., 2025) of naive, effector, memory, and exhausted CD8$^+$ T cells. Consensus ATACseq peaks were merged using GenomicRanges (Lawrence et al., 2013), and batch effects were corrected with ComBat-seq (Zhang et al., 2020). Differential accessibility was analyzed with DESeq2 (Love et al., 2014), and variance-stabilized counts (Love et al., 2014) were used for PCA. Developmental relationships were quantified based on Euclidean distances between tdT$^+$ group and reference centroids in PC space.

Transcription factor motif activity was quantified in R with chromVAR (Schep et al., 2017) using a fragments-in-peaks count matrix stored as a SummarizedExperiment with GenomicRanges. GC bias was corrected with chromVAR on genome BSgenome.Mmusculus.UCSC.mm10. Motif PWMs were taken from JASPAR2020 (vertebrates) and mapped to peaks with matchMotifs; motif activities (deviation scores and Z-scores) were computed with computeDeviations, and motif variability with computeVariability. For visualization, we curated a CD8 state–relevant TF panel. Deviation scores for selected motifs and groups of interest (NDLN/DLN/TUMOR, tdT/LAG3 strata) were quantile-normalized across samples and row-scaled and displayed as a heatmap with ComplexHeatmap (Gu, 2022) package.

Statistical methods

Statistical methods were conducted using Prism Version 10 (GraphPad). Comparison of matched samples was calculated using paired *t* test (Fig. 2 F; Fig. S2, H and I; Fig. S4 C; and Fig. S5 C). Comparisons of independent samples was calculated using unpaired *t* test (Fig. 1, C and D; Fig. 5 B, Fig. S1, A–D; and Fig. S4, D and F–G). Comparison of samples across time points was done using one-way ANOVA (Fig. S4 A) and two-way ANOVA (Figs. 2, B, C, H, and I; Fig. 5, C and F; Fig. S2, B, D, and F; and Fig. S5 B). Tumor growth curves were compared using a mixed-effects analysis (Fig. 5 I). Comparisons of ATACseq samples were calculated using Pearson correlation coefficient (Fig. 4 B). "*n*" represents the number of mice or patients analyzed in an experiment, with number of individual experiments listed in the legend. Samples are shown with the mean with or without error bars indicating SEM. Significance was defined as P = 0.05.

The key resources table is provided in Table S1.

Materials availability

The mouse lines generated in this study are available from the Vignali lab via a standard MTA. Further requests for the mouse lines should be directed to and will be provided by the lead contact, D.A.A. Vignali (dvignali@pitt.edu).

Online supplemental material

Fig. S1 shows supporting data for Figs. 1 and 2, including validation of the fidelity and specificity of the *Lag3*^{iCreERT2} *Rosa26*$^{LSL\text{-}tdT}$ fate mapping system and characterization of tdT$^+$ T cell subsets. Fig. S2 shows supporting data for Fig. 2, including the kinetics of LAG3$^+$tdT$^+$ and LAG3$^-$ tdT$^+$ CD8$^+$ T cells across multiple tumor models and the antigen-specific accumulation of tdT$^+$ cells in antigen-matched tumors. Fig. S3 shows supporting data for Figs. 3 and 4, including the transcriptional, clonal, and epigenetic relationships between LAG3$^+$tdT$^+$ and LAG3$^-$ tdT$^+$ CD8$^+$ T cell subsets. Fig. S4 shows supporting data for Fig. 5, including the persistence of circulating LAG3$^-$ tdT$^+$ cells in both monoclonal and polyclonal systems and their antigen-specific expansion following tumor rechallenge. Fig. S5 shows supporting data for Fig. 5, including the exhaustion phenotype of LAG3$^-$ tdT$^+$ cells and efficient diphtheria toxin–mediated depletion of

this population after secondary rechallenge. Table S1 contains the key resources table.

Data availability

This paper does not report original code. All sequencing data generated in this study, including scRNAseq, CITEseq (gene expression, Feature Barcode, and V(D)J TCR), and ATACseq datasets, are available through the NCBI Gene Expression Omnibus under accession number GSE337902 and will be publicly available upon publication. All data reported in this paper will be shared by the lead contact upon request. Any additional information required to reanalyze the data reported in this paper is available from the lead contact upon request.

Acknowledgments

The authors would like to thank the Vignali lab (https://www.vignali-lab.com/; @Vignali_Lab) for discussions and critically reading the manuscript. We thank Dewayne Falkner, Nicole Renne Brandon, Nan Shen, Nevil Abraham, and Heidi Gunzelman from the Immunology Flow Core for cell sorting and the staff of the Division of Laboratory Animal Services at the University of Pittsburgh for the animal husbandry. This work benefitted from SPECIAL BD LSRFORTESSA and used the University of Pittsburgh School of Medicine Unified Flow Core funded by National Institutes of Health (NIH) grant S10 OD011925-01. We thank the NIH Tetramer Core Facility (contract number 75N93020D00005) for providing D^b-gp100$^+$ tetramers. This research was supported in part by the University of Pittsburgh Center for Research Computing, RRID:SCR_022735, through the resources provided. Specifically, this work used the HTC cluster, which is supported by NIH award number S10OD028483.

This study was supported by the National Institutes of Health (NIH): P01 AI108545 to D.A.A. Vignali and E.J. Wherry; CA263850 to D.A.A. Vignali; AI144422 to D.A.A. Vignali and C.J.Workman; and AI155577, AI115712, AI117950, AI082630, and CA210944 to E.J. Wherry. Work in the Wherry lab is also supported by the Parker Institute for Cancer Immunotherapy, which supports the Cancer Immunology program at the University of Pennsylvania.

Author contributions: Vaishali Aggarwal: conceptualization, data curation, formal analysis, investigation, methodology, project administration, software, validation, visualization, and writing—original draft, review, and editing. Yangxi Sun: conceptualization, data curation, formal analysis, investigation, project administration, resources, validation, visualization, and writing— original draft, review, and editing. Chang Liu: conceptualization, formal analysis, investigation, visualization, and writing—review and editing. Jian Cui: Data curation, formal analysis, visualization, and writing—review and editing. Sasikanth Manne: formal analysis. Yingtong Dou: investigation. Qiang Chen: investigation. Erin A. Brunazzi: project administration, resources, and writing—review and editing. Kate M. Vignali: investigation, methodology, resources, and writing—review and editing. Haiguang Wang: data curation, funding acquisition, investigation, methodology, and writing—review and editing. E. John Wherry: funding acquisition and writing—review and editing. Creg J. Workman: conceptualization, funding acquisition, methodology, project administration, supervision, validation, and writing—original draft, review, and editing, Dario A.A. Vignali: conceptualization, funding acquisition, project administration, resources, supervision, and writing—review and editing.

Disclosures: E.J. Wherry reported personal fees from Arsenal Biosciences, Arpelos Biosciences, Marengo Therapeutics, New Limit, Synthekine, Coherus, Santa Ana, and Absci outside the submitted work. C.J. Workman reported a patent number 8551481 licensed (BMS). D.A.A. Vignali reported personal fees from Novasenta, Werewolf, BMS, Apeximmune, T7/Imreg Bio, Secarna, Third Arc Bio, Curie Bio, Abilytics, and Radionetics Oncology; and other from Novasenta, Trishula, and Werewolf outside the submitted work. In addition, D.A.A. Vignali had a patent to Immunomodulatory Peptides issued, a patent to LAG3 with royalties paid (BMS), a patent to IL-35 with royalties paid (Tizona), and a patent to NRP1 with royalties paid (Potenza). No other disclosures were reported.

Submitted: 23 October 2024
Revised: 25 November 2025
Accepted: 15 July 2026

References

Abdel-Hakeem, M.S., S. Manne, J.C. Beltra, E. Stelekati, Z. Chen, K. Nzingha, M.A. Ali, J.L. Johnson, J.R. Giles, D. Mathew, et al. 2021. Epigenetic scarring of exhausted T cells hinders memory differentiation upon eliminating chronic antigenic stimulation. *Nat. Immunol.* 22:1008–1019. https://doi.org/10.1038/s41590-021-00975-5

Aggarwal, V., C.J. Workman, and D.A.A. Vignali. 2023. LAG-3 as the third checkpoint inhibitor. *Nat. Immunol.* 24:1415–1422. https://doi.org/10.1038/s41590-023-01569-z

Andrews, L.P., A.R. Cillo, L. Karapetyan, J.M. Kirkwood, C.J. Workman, and D.A.A. Vignali. 2022. Molecular pathways and mechanisms of LAG3 in cancer therapy. *Clin. Cancer Res.* 28:5030–5039. https://doi.org/10.1158/1078-0432.CCR-21-2390

Andrews, L.P., A.E. Marciscano, C.G. Drake, and D.A. Vignali. 2017. LAG3 (CD223) as a cancer immunotherapy target. *Immunol. Rev.* 276:80–96. https://doi.org/10.1111/imr.12519

Andrews, L.P., A. Somasundaram, J.M. Moskovitz, A.L. Szymczak-Workman, C. Liu, A.R. Cillo, H. Lin, D.P. Normolle, K.D. Moynihan, I. Taniuchi, et al. 2020. Resistance to PD1 blockade in the absence of metalloprotease-mediated LAG3 shedding. *Sci. Immunol.* 5:eabc2728. https://doi.org/10.1126/sciimmunol.abc2728

Angelosanto, J.M., S.D. Blackburn, A. Crawford, and E.J. Wherry. 2012. Progressive loss of memory T cell potential and commitment to exhaustion during chronic viral infection. *J. Virol.* 86:8161–8170. https://doi.org/10.1128/JVI.00889-12

Baessler, A., and D.A.A. Vignali. 2024. T cell exhaustion. *Annu. Rev. Immunol.* 42:179–206. https://doi.org/10.1146/annurev-immunol-090222-110914

Beltra, J.C., S. Manne, M.S. Abdel-Hakeem, M. Kurachi, J.R. Giles, Z. Chen, V. Casella, S.F. Ngiow, O. Khan, Y.J. Huang, et al. 2020. Developmental relationships of four exhausted CD8$^+$ T cell subsets reveals underlying transcriptional and epigenetic landscape control mechanisms. *Immunity*. 52:825–841.e8. https://doi.org/10.1016/j.immuni.2020.04.014

Blackburn, S.D., H. Shin, W.N. Haining, T. Zou, C.J. Workman, A. Polley, M.R. Betts, G.J. Freeman, D.A.A. Vignali, and E.J. Wherry. 2009. Coregulation of CD8+ T cell exhaustion by multiple inhibitory receptors during chronic viral infection. *Nat. Immunol.* 10:29–37. https://doi.org/10.1038/ni.1679

Blank, C.U., W.N. Haining, W. Held, P.G. Hogan, A. Kallies, E. Lugli, R.C. Lynn, M. Philip, A. Rao, N.P. Restifo, et al. 2019. Defining 'T cell

exhaustion'. *Nat. Rev. Immunol.* 19:665–674. https://doi.org/10.1038/s41577-019-0221-9
Bordon, Y. 2019. TOX for tired T cells. *Nat. Rev. Immunol.* 19:476. https://doi.org/10.1038/s41577-019-0193-9
Buchholz, V.R., T.N. Schumacher, and D.H. Busch. 2016. T cell fate at the single-cell level. *Annu. Rev. Immunol.* 34:65–92. https://doi.org/10.1146/annurev-immunol-032414-112014
Chen, Z., Z. Ji, S.F. Ngiow, S. Manne, Z. Cai, A.C. Huang, J. Johnson, R.P. Staupe, B. Bengsch, C. Xu, et al. 2019. TCF-1-Centered transcriptional network drives an effector versus exhausted CD8 T cell-fate decision. *Immunity*. 51:840–855.e5. https://doi.org/10.1016/j.immuni.2019.09.013
Connolly, K.A., M. Kuchroo, A. Venkat, A. Khatun, J. Wang, I. William, N.I. Hornick, B.L. Fitzgerald, M. Damo, M.Y. Kasmani, et al. 2021. A reservoir of stem-like CD8$^+$ T cells in the tumor-draining lymph node preserves the ongoing antitumor immune response. *Sci. Immunol.* 6: eabg7836. https://doi.org/10.1126/sciimmunol.abg7836
Daniel, B., K.E. Yost, S. Hsiung, K. Sandor, Y. Xia, Y. Qi, K.J. Hiam-Galvez, M. Black, J.R. C, Q. Shi, et al. 2022. Divergent clonal differentiation trajectories of T cell exhaustion. *Nat. Immunol.* 23:1614–1627. https://doi.org/10.1038/s41590-022-01337-5
DePeaux, K., and G.M. Delgoffe. 2021. Metabolic barriers to cancer immunotherapy. *Nat. Rev. Immunol.* 21:785–797. https://doi.org/10.1038/s41577-021-00541-y
Giles, J.R., S.F. Ngiow, S. Manne, A.E. Baxter, O. Khan, P. Wang, R. Staupe, M.S. Abdel-Hakeem, H. Huang, D. Mathew, et al. 2022. Shared and distinct biological circuits in effector, memory and exhausted CD8$^+$ T cells revealed by temporal single-cell transcriptomics and epigenetics. *Nat. Immunol.* 23:1600–1613. https://doi.org/10.1038/s41590-022-01338-4
Grosso, J.F., M.V. Goldberg, D. Getnet, T.C. Bruno, H.R. Yen, K.J. Pyle, E. Hipkiss, D.A. Vignali, D.M. Pardoll, and C.G. Drake. 2009. Functionally distinct LAG-3 and PD-1 subsets on activated and chronically stimulated CD8 T cells. *J. Immunol.* 182:6659–6669. https://doi.org/10.4049/jimmunol.0804211
Grosso, J.F., C.C. Kelleher, T.J. Harris, C.H. Maris, E.L. Hipkiss, A. De Marzo, R. Anders, G. Netto, D. Getnet, T.C. Bruno, et al. 2007. LAG-3 regulates CD8+ T cell accumulation and effector function in murine self- and tumor-tolerance systems. *J. Clin. Invest.* 117:3383–3392. https://doi.org/10.1172/JCI31184
Gu, Z. 2022. Complex heatmap visualization. *Imeta*. 1:e43. https://doi.org/10.1002/imt2.43
Gu, Z., L. Gu, R. Eils, M. Schlesner, and B. Brors. 2014. circlize Implements and enhances circular visualization in R. *Bioinformatics*. 30:2811–2812. https://doi.org/10.1093/bioinformatics/btu393
Hao, Y., T. Stuart, M.H. Kowalski, S. Choudhary, P. Hoffman, A. Hartman, A. Srivastava, G. Molla, S. Madad, C. Fernandez-Granda, and R. Satija. 2024. Dictionary learning for integrative, multimodal and scalable single-cell analysis. *Nat. Biotechnol.* 42:293–304. https://doi.org/10.1038/s41587-023-01767-y
Honda, K., and D.R. Littman. 2016. The microbiota in adaptive immune homeostasis and disease. *Nature*. 535:75–84. https://doi.org/10.1038/nature18848
Huang, H., A.E. Baxter, Z. Zhang, C.R. Good, K.A. Alexander, Z. Chen, P.A.A. Garcia, P. Samareh, S.M. Collins, K.M. Glastad, et al. 2025. Deciphering the role of histone modifications in memory and exhausted CD8 T cells. *Sci. Rep.* 15:17359. https://doi.org/10.1038/s41598-025-99804-0
Huang, Q., X. Wu, Z. Wang, X. Chen, L. Wang, Y. Lu, D. Xiong, Q. Liu, Y. Tian, H. Lin, et al. 2022. The primordial differentiation of tumor-specific memory CD8$^+$ T cells as bona fide responders to PD-1/PD-L1 blockade in draining lymph nodes. *Cell*. 185:4049–4066.e25. https://doi.org/10.1016/j.cell.2022.09.020
Hudson, W.H., J. Gensheimer, M. Hashimoto, A. Wieland, R.M. Valanparambil, P. Li, J.X. Lin, B.T. Konieczny, S.J. Im, G.J. Freeman, et al. 2019. Proliferating transitory T cells with an effector-like transcriptional signature emerge from PD-1$^+$ stem-like CD8$^+$ T cells during chronic infection. *Immunity*. 51:1043–1058.e4. https://doi.org/10.1016/j.immuni.2019.11.002
Im, S.J., M. Hashimoto, M.Y. Gerner, J. Lee, H.T. Kissick, M.C. Burger, Q. Shan, J.S. Hale, J. Lee, T.H. Nasti, et al. 2016. Defining CD8+ T cells that provide the proliferative burst after PD-1 therapy. *Nature*. 537:417–421. https://doi.org/10.1038/nature19330
Khan, O., J.R. Giles, S. McDonald, S. Manne, S.F. Ngiow, K.P. Patel, M.T. Werner, A.C. Huang, K.A. Alexander, J.E. Wu, et al. 2019. TOX transcriptionally and epigenetically programs CD8$^+$ T cell exhaustion. *Nature*. 571:211–218. https://doi.org/10.1038/s41586-019-1325-x
Korsunsky, I., N. Millard, J. Fan, K. Slowikowski, F. Zhang, K. Wei, Y. Baglaenko, M. Brenner, P.R. Loh, and S. Raychaudhuri. 2019. Fast, sensitive and accurate integration of single-cell data with Harmony. *Nat. Methods*. 16:1289–1296. https://doi.org/10.1038/s41592-019-0619-0
Kurd, N.S., Z. He, T.L. Louis, J.J. Milner, K.D. Omilusik, W. Jin, M.S. Tsai, C.E. Widjaja, J.N. Kanbar, J.G. Olvera, et al. 2020. Early precursors and molecular determinants of tissue-resident memory CD8$^+$ T lymphocytes revealed by single-cell RNA sequencing. *Sci. Immunol.* 5:eaaz6894. https://doi.org/10.1126/sciimmunol.aaz6894
Lawrence, M., W. Huber, H. Pages, P. Aboyoun, M. Carlson, R. Gentleman, M.T. Morgan, and V.J. Carey. 2013. Software for computing and annotating genomic ranges. *PLoS Comput. Biol.* 9:e1003118. https://doi.org/10.1371/journal.pcbi.1003118
Liu, C., A. Somasundaram, S. Manne, A.M. Gocher, A.L. Szymczak-Workman, K.M. Vignali, E.N. Scott, D.P. Normolle, E. John Wherry, E.J. Lipson, et al. 2020. Neuropilin-1 is a T cell memory checkpoint limiting long-term antitumor immunity. *Nat. Immunol.* 21:1010–1021. https://doi.org/10.1038/s41590-020-0733-2
Liu, Z., Y. Zhang, N. Ma, Y. Yang, Y. Ma, F. Wang, Y. Wang, J. Wei, H. Chen, A. Tartarone, et al. 2023. Progenitor-like exhausted SPRY1$^+$CD8$^+$ T cells potentiate responsiveness to neoadjuvant PD-1 blockade in esophageal squamous cell carcinoma. *Cancer Cell*. 41:1852–1870.e9. https://doi.org/10.1016/j.ccell.2023.09.011
Love, M.I., W. Huber, and S. Anders. 2014. Moderated estimation of fold change and dispersion for RNA-seq data with DESeq2. *Genome Biol.* 15: 550. https://doi.org/10.1186/s13059-014-0550-8
Lucas, C.L., C.J. Workman, S. Beyaz, S. LoCascio, G. Zhao, D.A.A. Vignali, and M. Sykes. 2011. LAG-3, TGF-β, and cell-intrinsic PD-1 inhibitory pathways contribute to CD8 but not CD4 T-cell tolerance induced by allogeneic BMT with anti-CD40L. *Blood*. 117:5532–5540. https://doi.org/10.1182/blood-2010-11-318675
McLane, L.M., M.S. Abdel-Hakeem, and E.J. Wherry. 2019. CD8 T cell exhaustion during chronic viral infection and cancer. *Annu. Rev. Immunol.* 37:457–495. https://doi.org/10.1146/annurev-immunol-041015-055318
Miller, B.C., D.R. Sen, R. Al Abosy, K. Bi, Y.V. Virkud, M.W. LaFleur, K.B. Yates, A. Lako, K. Felt, G.S. Naik, et al. 2019. Subsets of exhausted CD8$^+$ T cells differentially mediate tumor control and respond to checkpoint blockade. *Nat. Immunol.* 20:326–336. https://doi.org/10.1038/s41590-019-0312-6
Paley, M.A., D.C. Kroy, P.M. Odorizzi, J.B. Johnnidis, D.V. Dolfi, B.E. Barnett, E.K. Bikoff, E.J. Robertson, G.M. Lauer, S.L. Reiner, and E.J. Wherry. 2012. Progenitor and terminal subsets of CD8+ T cells cooperate to contain chronic viral infection. *Science*. 338:1220–1225. https://doi.org/10.1126/science.1229620
Pauken, K.E., M.A. Sammons, P.M. Odorizzi, S. Manne, J. Godec, O. Khan, A.M. Drake, Z. Chen, D.R. Sen, M. Kurachi, et al. 2016. Epigenetic stability of exhausted T cells limits durability of reinvigoration by PD-1 blockade. *Science*. 354:1160–1165. https://doi.org/10.1126/science.aaf2807
Philip, M., and A. Schietinger. 2022. CD8$^+$ T cell differentiation and dysfunction in cancer. *Nat. Rev. Immunol.* 22:209–223. https://doi.org/10.1038/s41577-021-00574-3
Sade-Feldman, M., K. Yizhak, S.L. Bjorgaard, J.P. Ray, C.G. de Boer, R.W. Jenkins, D.J. Lieb, J.H. Chen, D.T. Frederick, M. Barzily-Rokni, et al. 2019. Defining T cell states associated with response to checkpoint immunotherapy in melanoma. *Cell*. 175:404. https://doi.org/10.1016/j.cell.2018.12.034
Satpathy, A.T., J.M. Granja, K.E. Yost, Y. Qi, F. Meschi, G.P. McDermott, B.N. Olsen, M.R. Mumbach, S.E. Pierce, M.R. Corces, et al. 2019. Massively parallel single-cell chromatin landscapes of human immune cell development and intratumoral T cell exhaustion. *Nat. Biotechnol.* 37: 925–936. https://doi.org/10.1038/s41587-019-0206-z
Schep, A.N., B. Wu, J.D. Buenrostro, and W.J. Greenleaf. 2017. chromVAR: inferring transcription-factor-associated accessibility from single-cell epigenomic data. *Nat. Methods*. 14:975–978. https://doi.org/10.1038/nmeth.4401
Schietinger, A., M. Philip, V.E. Krisnawan, E.Y. Chiu, J.J. Delrow, R.S. Basom, P. Lauer, D.G. Brockstedt, S.E. Knoblaugh, G.J. Hämmerling, et al. 2016. Tumor-specific T cell dysfunction is a dynamic antigen-driven differentiation program initiated early during tumorigenesis. *Immunity*. 45: 389–401. https://doi.org/10.1016/j.immuni.2016.07.011
Sen, D.R., J. Kaminski, R.A. Barnitz, M. Kurachi, U. Gerdemann, K.B. Yates, H.W. Tsao, J. Godec, M.W. LaFleur, F.D. Brown, et al. 2016. The epigenetic landscape of T cell exhaustion. *Science*. 354:1165–1169. https://doi.org/10.1126/science.aae0491

Siddiqui, I., K. Schaeuble, V. Chennupati, S.A. Fuertes Marraco, S. Calderon-Copete, D. Pais Ferreira, S.J. Carmona, L. Scarpellino, D. Gfeller, S. Pradervand, et al. 2019. Intratumoral Tcf1^{+}PD-1^{+}CD8^{+} T cells with stem-like properties promote tumor control in response to vaccination and checkpoint blockade immunotherapy. *Immunity*. 50:195–211.e10. https://doi.org/10.1016/j.immuni.2018.12.021

Song, L., D. Cohen, Z. Ouyang, Y. Cao, X. Hu, and X.S. Liu. 2021. TRUST4: Immune repertoire reconstruction from bulk and single-cell RNA-seq data. *Nat. Methods*. 18:627–630. https://doi.org/10.1038/s41592-021-01142-2

Szymczak, A.L., C.J. Workman, Y. Wang, K.M. Vignali, S. Dilioglou, E.F. Vanin, and D.A. Vignali. 2004. Correction of multi-gene deficiency in vivo using a single 'self-cleaving' 2A peptide-based retroviral vector. *Nat. Biotechnol.* 22:589–594. https://doi.org/10.1038/nbt957

Tawbi, H.A., D. Schadendorf, E.J. Lipson, P.A. Ascierto, L. Matamala, E. Castillo Gutierrez, P. Rutkowski, H.J. Gogas, C.D. Lao, J.J. De Menezes, et al. 2022. Relatlimab and Nivolumab versus Nivolumab in Untreated advanced melanoma. *N. Engl. J. Med.* 386:24–34. https://doi.org/10.1056/NEJMoa2109970

Utzschneider, D.T., M. Charmoy, V. Chennupati, L. Pousse, D.P. Ferreira, S. Calderon-Copete, M. Danilo, F. Alfei, M. Hofmann, D. Wieland, et al. 2016. T cell factor 1-expressing memory-like CD8(+) T cells sustain the immune response to chronic viral infections. *Immunity*. 45:415–427. https://doi.org/10.1016/j.immuni.2016.07.021

Wherry, E.J., and M. Kurachi. 2015. Molecular and cellular insights into T cell exhaustion. *Nat. Rev. Immunol.* 15:486–499. https://doi.org/10.1038/nri3862

Woo, S.-R., M.E. Turnis, M.V. Goldberg, J. Bankoti, M. Selby, C.J. Nirschl, M.L. Bettini, D.M. Gravano, P. Vogel, C.L. Liu, et al. 2012. Immune inhibitory molecules LAG-3 and PD-1 synergistically regulate T-cell function to promote tumoral immune escape. *Cancer Res.* 72:917–927. https://doi.org/10.1158/0008-5472.CAN-11-1620

Yang, W., and Y. Cong. 2021. Gut microbiota-derived metabolites in the regulation of host immune responses and immune-related inflammatory diseases. *Cell. Mol. Immunol.* 18:866–877. https://doi.org/10.1038/s41423-021-00661-4

Yates, K.B., P. Tonnerre, G.E. Martin, U. Gerdemann, R. Al Abosy, D.E. Comstock, S.A. Weiss, D. Wolski, D.C. Tully, R.T. Chung, et al. 2021. Epigenetic scars of CD8^{+} T cell exhaustion persist after cure of chronic infection in humans. *Nat. Immunol.* 22:1020–1029. https://doi.org/10.1038/s41590-021-00979-1

Zhang, Y., G. Parmigiani, and W.E. Johnson. 2020. *ComBat-seq*: Batch effect adjustment for RNA-seq count data. *NAR Genom Bioinform*. 2:lqaa078. https://doi.org/10.1093/nargab/lqaa078

Zhou, P., H. Shi, H. Huang, X. Sun, S. Yuan, N.M. Chapman, J.P. Connelly, S.A. Lim, J. Saravia, A. Kc, et al. 2023. Single-cell CRISPR screens in vivo map T cell fate regulomes in cancer. *Nature*. 624:154–163. https://doi.org/10.1038/s41586-023-06733-x

JEM

Supplemental material

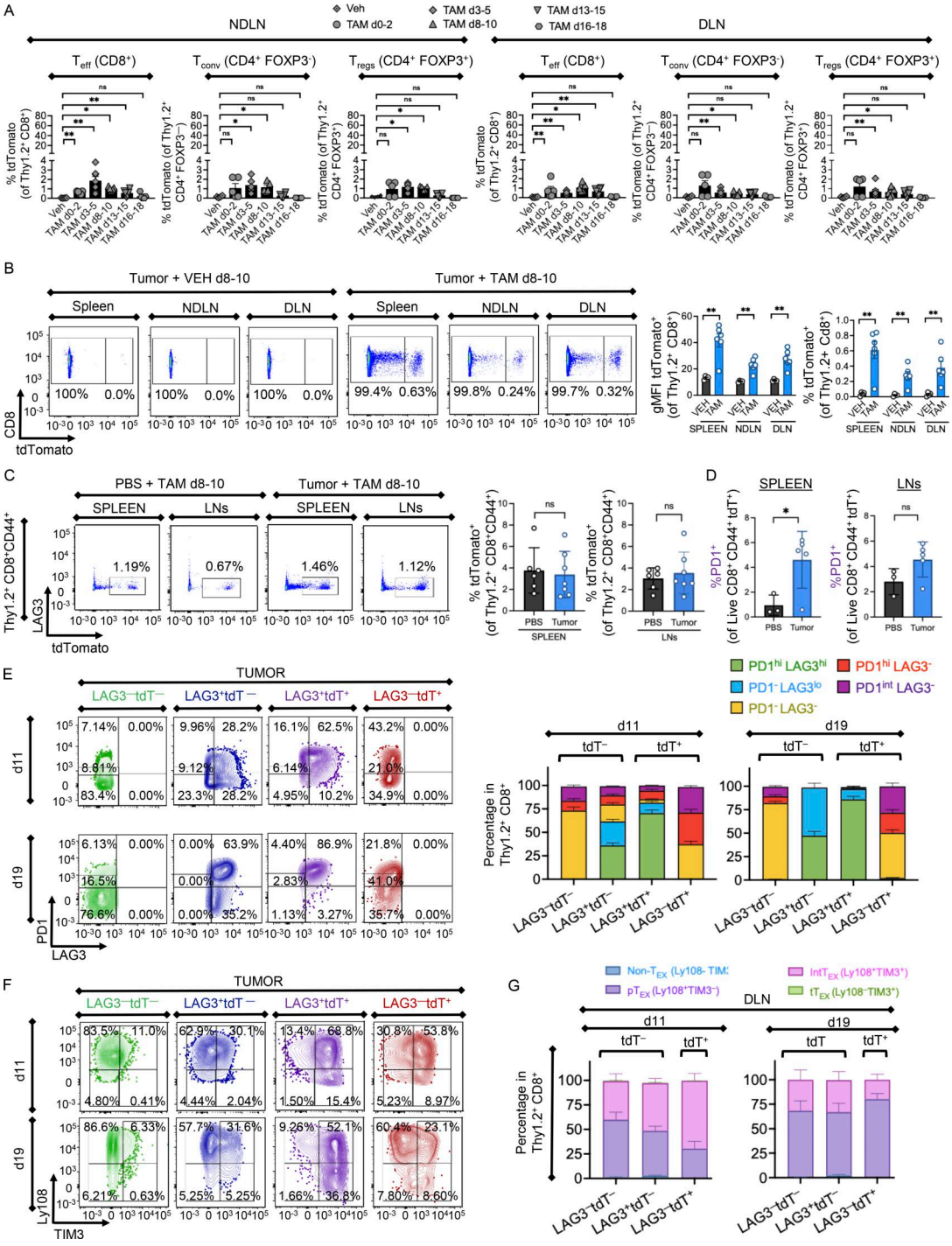

Figure S1. **Validation of a tamoxifen-inducible LAG3⁺ cell–specific Cre line. (A)** tdT expression was assessed on the CD8⁺, T_{conv} (CD4⁺ FOXP3⁻), and T_{reg} (CD4⁺ FOXP3⁺) T_{EX} cells from NDLNs (left panel) and DLNs (right panel) to evaluate labeling efficiency in respective T cell compartment with different tamoxifen treatment regimen. Gated on Thy1.2⁺ T cells. **(B)** *Lag3*^{iCreERT2} *Rosa26*$^{LSL\text{-}tdT}$ mice were implanted with 1.25 × 10⁵ B16-F10 cells i.d. and treated with three intraperitoneal tamoxifen injections (2 mg in 5% EtOH/sunflower oil) and oil control on d8–10. Harvested on d19. tdT expression was assessed on the CD8⁺ T cells isolated from spleen, NDLNs, and DLNs in the vehicle control versus tamoxifen-treated mice. **(C)** tdT expression was assessed on the CD8⁺ CD44⁺ T cells isolated from spleen and LNs in the mice injected with 1× PBS versus B16-F10 i.d. and treated with three intraperitoneal tamoxifen injections (2 mg in 5% EtOH/sunflower oil) d8–10. Harvested on d18. **(D)** PD1 expression was assessed on tdT⁺ cells from C. **(E)** PD1 and LAG3 expression on tdT subsets of tumor-infiltrating CD8⁺ T cells. Phylum plot represents the percentage of PD1^{hi}LAG3^{hi} (green), PD1⁻LAG3^{lo} (blue), PD1⁻LAG3⁻ (yellow), PD1^{hi}LAG3⁻ (red), and PD1^{int}LAG3⁻ (purple) CD8⁺ T cells. **(F)** Flow cytometry plots showing LY108 and TIM3 expression on tdT subsets of tumor-infiltrating CD8⁺ T cells. **(G)** Ly108 and TIM3 expression was assessed on LAG3⁻tdT⁻, LAG3⁺tdT⁻, and LAG3⁻ tdT⁺ CD8⁺ T cells in DLN on d11 and d19 from the *Lag3*^{iCreERT2} *Rosa26*$^{LSL\text{-}tdT}$ mice. Phylum plot represents the percentage of Ly108⁻TIM3⁻ (blue), Ly108⁺TIM3⁻ (purple), Ly108⁺TIM3⁺ (pink), and Ly108⁻TIM3⁺ (green) CD8⁺ T cells within those subsets. Data in A, B, E, and F are from *n* = 5–9 mice per group, pooled from three independent experiments. Data in C and D are representative of two independent experiments with *n* = 6–7 mice per group. *P < 0.05; **P < 0.01; ns, not significant by (A–D) unpaired *t* test. Error bars represent the mean ± SEM.

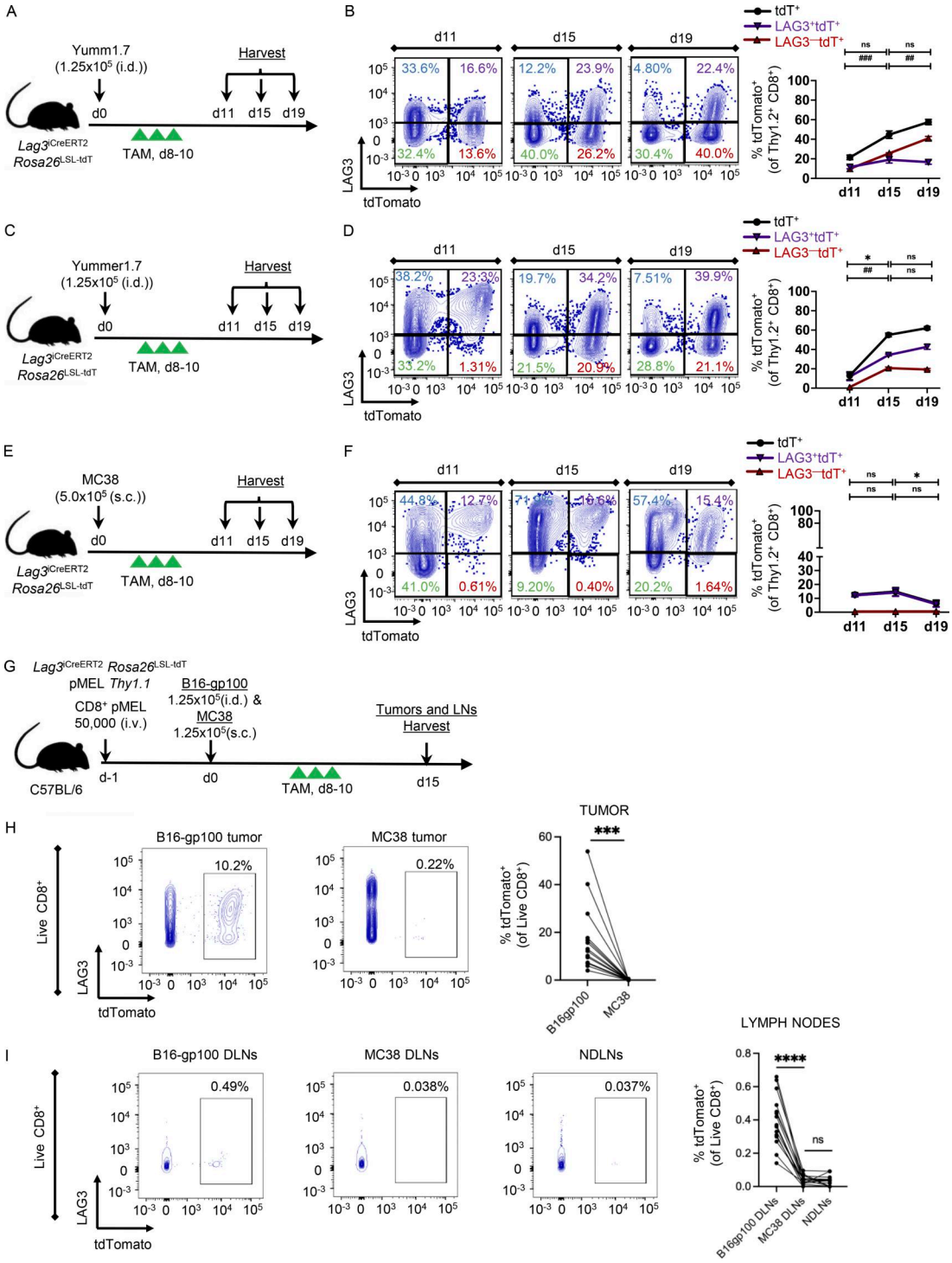

Figure S2. **Population kinetics of fate-mapped tdT⁺ CD8⁺ T cells across multiple tumor models. (A)** Scheme for evaluation of population kinetics of tdT⁺ cells in tumor models. *Lag3*^{iCreERT2} *Rosa26*$^{LSL\text{-}tdT}$ mice were i.d. implanted with melanoma cells (1.25×10^5), treated with three tamoxifen injections (2 mg in 5% EtOH/sunflower oil) at d8–10, and harvested on d11, d15, and d19. **(A–D)** LAG3 and tdT expression was assessed on CD8⁺ T cells isolated from (A and B) YUMM1.7 and (C and D) YUMMER1.7, gated on Thy1.2⁺ CD8⁺ T cells. **(E)** Scheme for evaluation of population kinetics of tdT⁺ cells in the MC38 colon adenocarcinoma model. *Lag3*^{iCreERT2} *Rosa26*$^{LSL\text{-}tdT}$ mice were s.c. implanted with MC38 cells (5.0×10^5), treated with three tamoxifen injections (2 mg in 5% EtOH/sunflower oil) at d8–10, and harvested on d11, d15, and d19. **(F)** LAG3 and tdT expression was assessed on CD8⁺ T cells isolated from E, gated on Thy1.2⁺ CD8⁺ T cells. **(G)** C57BL/6 mice received adoptive transfer of 50,000 *Lag3*^{iCreERT2}*Rosa26*$^{LSL\text{-}tdT}$ pMEL cells (i.v.) followed by dual tumor inoculation with B16gp100 (i.d.) and antigen-irrelevant MC38 (s.c.). Tamoxifen (2 mg in 5% EtOH/sunflower oil) was administered on d8–10. **(H and I)** LAG3 and tdT expression were then assessed in (H) tumors, (I) DLNs, and non-NDLNs. Data in B, D, and F are from *n* = 5–6 mice per group, pooled from three independent experiments. Data in H and I are representative of two independent experiments with *n* = 14 mice. Statistical analysis of LAG3⁺tdT⁺ and LAG3⁻tdT⁺ CD8⁺ T cells from d11–15 and d15–19 are represented by * and #, respectively. *P < 0.05; ***P < 0.001; ****P < 0.0001; ##P < 0.01; ###P < 0.001; ns, not significant, by two-way ANOVA (B, D, and F) and paired *t* test (H and I).

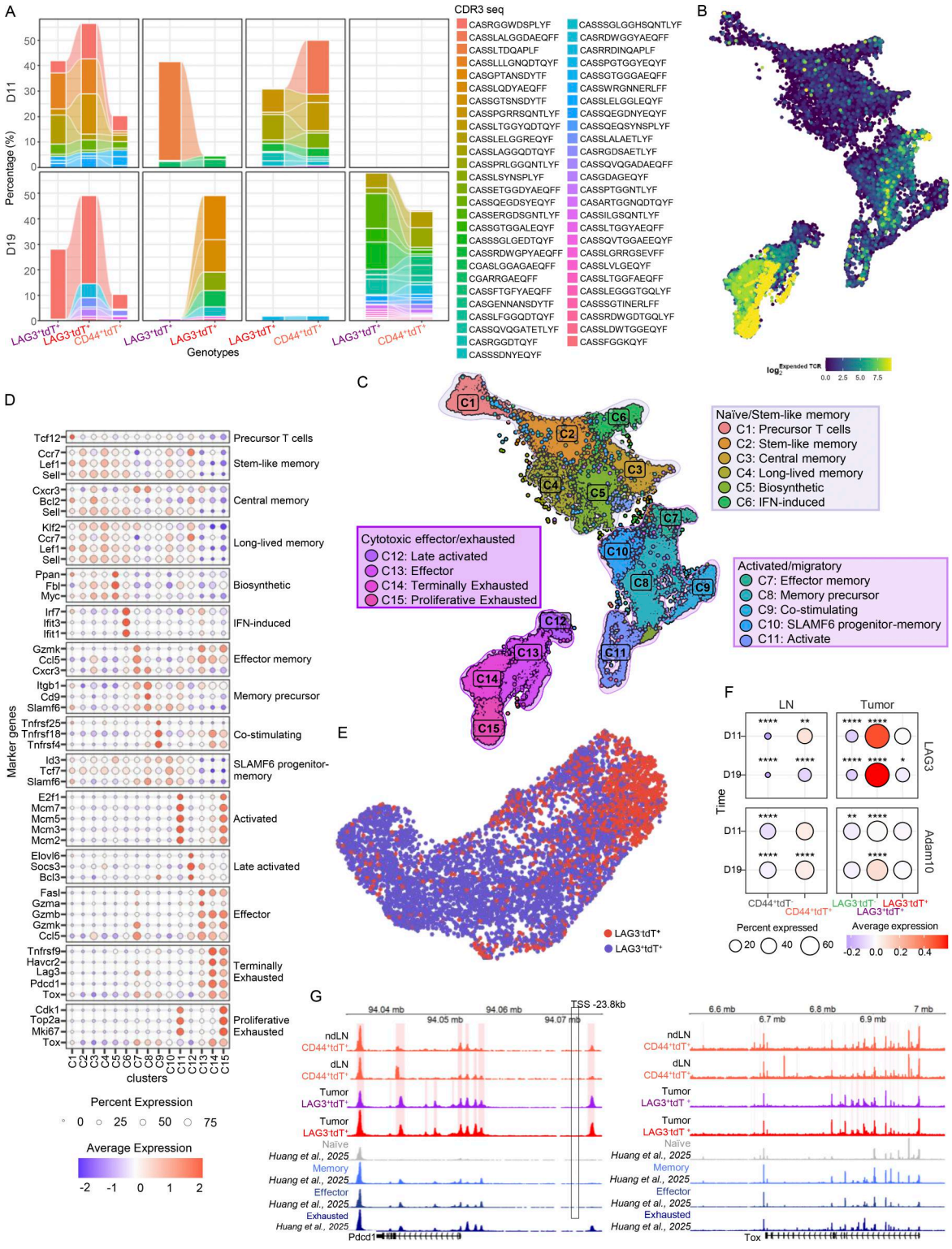

Figure S3. **Transcriptional, clonal, and epigenetic characterization of fate-mapped tdT⁺ CD8⁺ T cells. (A)** Stream plots showing distribution of commonly shared TCR among tdT⁺ subsets at d11 and d19, alongside representative CDR3 sequences. **(B)** UMAP embedding of CD8⁺ T cells overlaid with TCR distribution, heat-colored by the log-transformed abundance of expanded clones. **(C)** UMAP embedding of CD8⁺ T cells colored by transcriptional state, grouped into naive/memory, activated/migratory, and cytotoxic effector/exhausted partitions, with distinct clusters highlighted and defined within each partition. **(D)** Dot plot of representative gene signatures across transcriptional clusters. Dot size indicates percent expression; color indicates scaled average expression. **(E)** Distribution of LAG3⁻tdT⁺ and LAG3⁺tdT⁺ populations within tumor samples. **(F)** Expression levels of *Lag3* and *Adam10* in all tdT⁺ subsets in LNs and tumor at d11 and d19. **(G)** ATACseq accessibility tracks for *Pdcd1* and *Tox* across tdT subsets with external reference. Shown are aggregated ATACseq profiles for each loci aligned to reference datasets by Huang et al. (2025). Significantly accessible regions identified by differential accessibility analysis are highlighted. Data in A–G are representative of two independent experiments. *P < 0.05; **P < 0.01; ****P < 0.0001; by Wilcoxon rank-sum test (F).

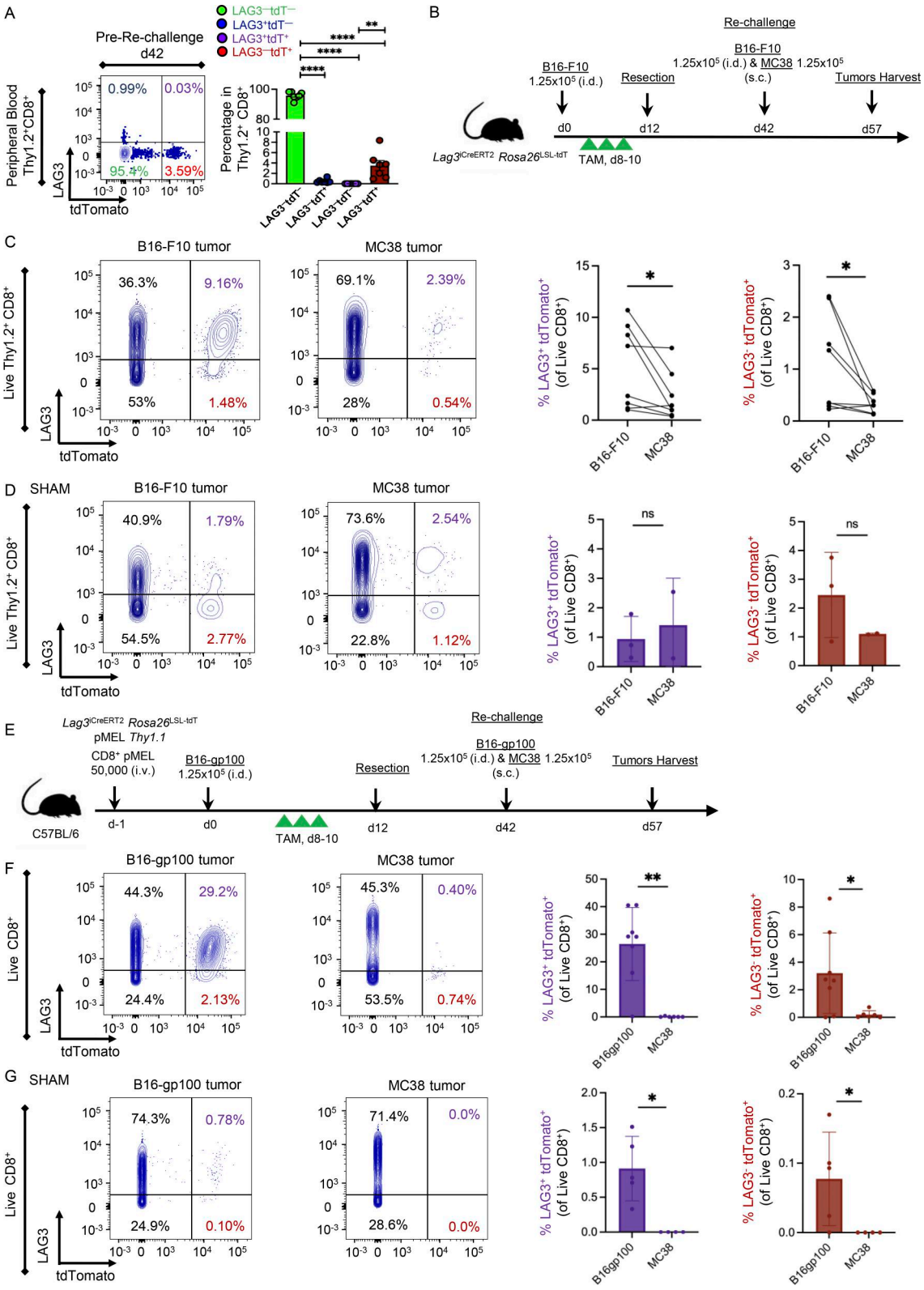

Figure S4. **Antigen-driven differentiation of circulating LAG3⁻tdT⁺ CD8⁺ T cells upon tumor rechallenge. (A)** LAG3 and tdT expression was assessed on the CD8⁺ T cells in peripheral blood before rechallenge on d42. **(B)** Scheme to evaluate the differentiation potential of circulating LAG3⁻tdT⁺ cells upon tumor rechallenge was designed to be antigen driven. **(C and D)** LAG3 and tdT expression were subsequently assessed in (C) tumors of experimental mice and (D) tumors of SHAM controls. **(E)** Scheme to evaluate the differentiation potential of circulating LAG3⁻tdT⁺ cells upon tumor rechallenge was designed to be antigen driven in the monoclonal setting. **(F and G)** LAG3 and tdT expression were subsequently assessed in (F) tumors of experimental mice and (G) tumors of SHAM controls. Data in A are representative of three independent experiments with $n = 8$ mice. Data in C, D, F, and G are from $n = 5–8$ mice per group, pooled from two independent experiments. *P < 0.05; **P < 0.01; ****P < 0.0001 by (A) one-way ANOVA, by (C) paired t test, and by (D, F, and G) unpaired t test.

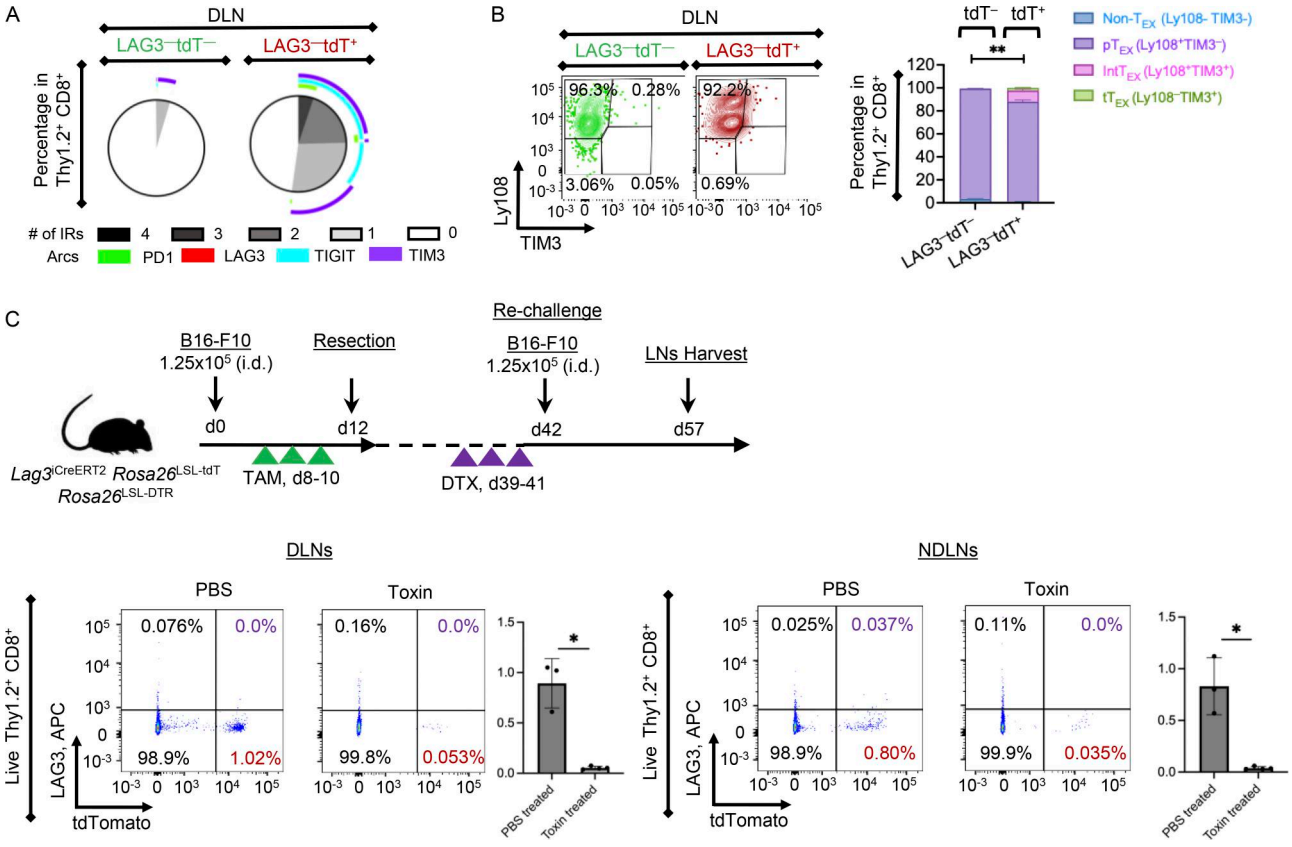

Figure S5. **Phenotypic analysis and depletion of circulaing LAG3⁻tdT⁺ CD8⁺ T cells. (A)** Spice plot visualization for co-expression of IRs (n = 4) on LAG3⁻tdT⁻ and LAG3⁻tdT⁺ CD8⁺ T cells in DLNs after B16-F10 rechallenge on d18. **(B)** Ly108 and TIM3 expression was assessed on LAG3⁻tdT⁻ (green) and LAG3⁻tdT⁺ (red) CD8⁺ T cells in DLNs after B16-F10 rechallenge on d18. Phylum plot represents the percentage of Ly108⁻TIM3⁻ (blue), Ly108⁺TIM3⁻ (purple), Ly108⁺TIM3⁺ (pink), and Ly108⁻TIM3⁺ (green) CD8⁺ T cells within LAG3⁻tdT⁻ and LAG3⁻tdT⁺ CD8⁺ T cells in DLNs. **(C)** Scheme to validate the deletion of LAG3⁻tdT⁺ cells. LAG3 and tdT expression was assessed on d57 for both DLNs and NDLNs. Data in A and B are representative of three independent experiments with n = 8 mice. Data in C are from n = 3–4 mice per group, pooled from two independent experiments. *P < 0.05; **P < 0.01 by (B) two-way ANOVA and by (C) paired t test. Error bars represent the mean + SEM.

Provided online is Table S1. Table S1 shows the key resources table.